

Comparing Direct and Indirect Thrust Measurements from Passively Fed Ionic Electrospray Thrusters

Daniel G. Courtney,^{*} Simon Dandavino,[†] and Herbert Shea[‡]
École Polytechnique Fédérale de Lausanne, CH-2002 Neuchâtel, Switzerland

DOI: 10.2514/1.B35836

Highly ionic beams of several hundred microampere per squared centimeter have been measured from porous glass ionic liquid electrospray sources fabricated using a conventional mill. The thrust output from three prototype devices, two emitting the ionic liquid 1-ethyl-3-methylimidazolium-bis(trifluoromethylsulfonyle)imide and one emitting 1-ethyl-3-methylimidazolium-tetrafluoroborate, was measured directly using a precise balance. Thrusts up to 50 μN were measured when emitting 1-ethyl-3-methylimidazolium-bis(trifluoromethylsulfonyle)imide in a bipolar, alternating potential configuration at less than 0.8 W input power and with propellant supplied from an internal reservoir. Measurements of mass spectra via time-of-flight spectrometry, angle resolved current distributions, ion fragmentation, and energy deficits have been applied to accurately calculate thrust and mass flow rates indirectly from the same devices. For two of the three cases, calculated and directly measured thrusts were in agreement to within a few micronewtons at input powers from 0.1 to 0.8 W. Emissions of 1-ethyl-3-methylimidazolium-tetrafluoroborate were shown to yield nearly purely ionic beams supporting high propulsive efficiencies and specific impulses of $\sim 65\%$ and greater than 3200 s, respectively, at 0.5 W. Conversely, greater polydispersity was observed in 1-ethyl-3-methylimidazolium-bis(trifluoromethylsulfonyle)imide emissions, contributing to reduced specific performance, $\sim 50\%$ propulsive efficiency, and ~ 1500 s specific impulse at 0.5 W.

Nomenclature

A	=	collector plate area, m^2
Da	=	unified atomic mass units
$F_{T/m}$	=	piecewise fragmentation modifiers to time-of-flight calculations
f_n	=	fraction due to species with solvation n
h	=	emitter height, μm
$I(t)$	=	time-of-flight collector current, A
I_b	=	beam current, A
I_c	=	ungated collected current, A
I_{em}	=	emitted current, A
I_{ex}	=	extractor grid current, A
I_{sp}	=	specific impulse, s
$j(\theta)$	=	collected current density, A/m^2
K_ξ	=	kinetic energy of species, ξ
L	=	time-of-flight flight distance
L_c	=	distance from the source to the collector, m
m_ξ	=	mass of species ξ , kg
\dot{m}	=	mass flow rate, kg/s
q	=	species charge, C
R_c	=	emitter apex radius of curvature, m
s	=	emitter apex to extractor grid separation, μm
T	=	calculated thrust, N
T_{DTM}	=	directly measured thrust, N
T_{ITM}	=	calculated, averaged bipolar thrust, N
T_{TOF}	=	thrust calculated by time of flight alone, N
t	=	flight time, s
t_ξ	=	flight time of species ξ , s
V_a	=	average beam potential, V
V_{em}	=	emitter voltage, V

V_{start}	=	estimated starting potential for emission, V
α	=	alternation duty cycle
γ	=	liquid surface tension, N/m
ΔV	=	energy deficit, V
η_{prop}	=	propulsive efficiency
θ	=	beam angle measured
θ_{eff}	=	effective beam angle
θ_0	=	beam angle offset
κ	=	time-of-flight thrust factor
ϕ	=	time-of-flight mass flow factor

I. Introduction

INTEREST in electrospray propulsion has seen a resurgence over the past decade with the advent of techniques for fabricating high-current density emission sources [1–5] and the performance benefits identified when employing room-temperature ionic liquids (ILs) as propellants [6–8]. IL electrosprays can yield highly ionic and monoenergetic beamlets, leading to high specific impulse and propulsive efficiency from inherently miniature emission sites (Taylor cones [9]). The thrust per IL emission site is small ($\sim 10 - 100$ nN); hence, challenges in achieving useful devices are associated with scaling up the total emission current while maintaining good specific performance. This need can be compared with, for example, plasma-based propulsion systems where difficulties in maintaining high power efficiency quickly arise when attempting to miniaturize (e.g., [10]). The technology is therefore well suited for small or distributable propulsion systems that require high Δv (velocity change), of which there is a growing need/interest yet a relative dearth of fully qualified systems [11,12].

Electrospray propulsion systems targeting the purely ionic regime (PIR) of emission from ILs, hereafter referred to as ionic liquid ion sources (ILISs) [7], are a particular niche, sharing functional similarities yet numerous benefits compared with both colloidal [13] and liquid-metal ion source (LMIS) [14,15] thrusters. The potential benefits of ILIS include the following:

- 1) The low surface tension of ILs leads to low operating voltages compared with LMIS.
- 2) ILs are liquid at room temperature, and therefore may not require heating.
- 3) Many ILs have negligible vapor pressure, enabling storage at vacuum.
- 4) Positive and negative ion emissions can be sustained, enabling charge neutralization without a dedicated neutralizer.

Received 8 April 2015; revision received 22 July 2015; accepted for publication 27 July 2015; published online 24 December 2015. Copyright © 2012 by the American Institute of Aeronautics and Astronautics, Inc. All rights reserved. Copies of this paper may be made for personal or internal use, on condition that the copier pay the \$10.00 per-copy fee to the Copyright Clearance Center, Inc., 222 Rosewood Drive, Danvers, MA 01923; include the code 1533-3876/15 and \$10.00 in correspondence with the CCC.

^{*}Postdoctoral Researcher, EPFL-IMT-LMTS, Microsystems for Space Technologies Laboratory; dcourtney@alum.mit.edu. Member AIAA.

[†]Deputy Director, EPFL-eSpace, Microsystems for Space Technologies Laboratory.

[‡]Associate Professor, EPFL-IMT-LMTS, Microsystems for Space Technologies Laboratory.

5) High specific impulses that are in excess of 3000 s [16], and propulsive efficiencies near 90% [8].

6) The inherent low flow rates can be accommodated through passive feeding alone [2,7,17].

The later feature could greatly reduce the mass, power, and volume requirements of a thruster by obviating the need for pumps, valves, and propellant pressurization systems.

In this paper, we present a simple-to-fabricate form of an ILIS and demonstrate, through both direct and indirect thrust measurements, that tens of micronewton thrust levels and good specific performance can be achieved from a small (16 g, $\sim 3.7 \times 3.7 \times 0.8$ cm) device wherein propellant is supplied to emission sites passively.

The low absolute thrusts (approximately tens of micronewtons) yet relatively high system masses [18] of electrospray thrusters can present challenges when attempting to obtain direct thrust measurements using a dedicated balance or other force transducer, leading to few examples in the literature. In [18], precise measurements and corresponding indirect calculations were presented for a colloidal thruster. However, [16] presented the only instance of a DTM from a passively fed ILIS known to the authors. That study confirmed that thrusts of $\sim 0.1 \mu\text{N}/\mu\text{A}$ can be achieved from arrays of ILISs and that these levels are close to those expected by extrapolation of indirect calculations based on individual emitter measurements. In Sec. V, we present both direct thrust measurements and a collection of probe measurements from the same devices, enabling the thrust to be calculated indirectly for comparison.

Indirect thrust measurements (ITMs) by time-of-flight (TOF) spectrometry [19–22] are often applied to calculate expected performance. TOF measurements, which account for the spread in species charge to mass ratio within the beam, are suitable for providing a foundation for performance due to the potential diversity of particles emitted from electrospray sources. However, other factors such as energy deficits, the angular beam distribution, electrode impingements, and ion fragmentation may alter the output to a measurable degree. In Sec. II, we arrive at performance expressions derived from a series of measurements targeting each of these factors. Subsequently, in Secs. V and VI, we present and discuss a comparison between DTMs and ITMs as calculated using this approach.

Several groups have targeted high-current-density passively fed ILISs, which can provide tens of micronewtons of thrust per squared centimeter or, equivalently, approximately hundreds of microamperes per squared centimeter. Depending on the type and geometry of ILIS emitter structures, each emitter may support multiple emission sites (presumably stable Taylor cones) and yield from ~ 0.1 [7] to greater than $5 \mu\text{A}$ [17,23] of emission current. To generate sufficiently strong electric fields for emission while facilitating liquid transport [24], structures $\sim 100 \mu\text{m}$ tall and terminated by an apex radius or capillary orifice close to $10 \mu\text{m}$ have been targeted. Such dimensions are well within the capabilities of numerous microfabrication techniques, leading to a myriad of approaches. These include silicon capillaries [3,4,25,26], silicon tips roughened through etches or carbon nanotube (CNT) growth [1,17], electrochemical etching of porous metals [16,27], use of Rosensweig instabilities in ionic liquid ferrofluids [28], and laser ablation of porous glass [5].

Arrays of externally wetted [17] and porous [2,5] ILISs have, encouragingly, been demonstrated to support a few hundred microamperes per centimeter squared of highly ionic emissions. Porous substrates are particularly advantageous in that they inherently provide a simple and integral flowpath from a rear-mounted and hydraulically coupled reservoir, enabling simple capillary-driven and zero-gravity compatible passive feeding. In contrast, externally wetted arrays have, to date, been operated from a drop of liquid placed on the surface, with a continuous passive flow supply yet to be demonstrated.

We have identified and exploited two critical traits of recently demonstrated porous emitter arrays in developing a unique low-cost fabrication technique:

First, compared with precise silicon microfabrication [26], the tendency for porous emitters to achieve high and ionic currents is particularly remarkable considering the relative imprecision and range in apex radii typical of processes that have successfully been

applied (e.g., few to tens of micrometers in [27]). In porous materials, the Taylor cone base diameter likely scales with the characteristic length scale of the reservoir pore's Laplace pressure, leading to observations of multiple, small emission sites from each emitting structure [24]. Although these trends require further understanding, the behavior is indicative of an apparent decoupling between the fluidic transport geometry (the pores) and that determining the electrostatic field (the emitter) when using porous structures. If a shape can be fabricated to yield sufficiently high fields to establish emission sites localized to pores, highly ionic and high-current beams have tended to follow, including at multiple points on each structure.

Second, the high conductivities and moderate dielectric constants of ILs enable emission from nonconductive glass structures [5,29]. Furthermore, the brittle nature of porous glass enables abrasive machining with reduced risk of sealing surface pores, as could result with relatively malleable porous metals.

Figure 1 presents an overview of the emitter geometry and functional configuration applied here. In lieu of individual micro-fabricated emitters, a small conventional computer numerical control (CNC) mill was used to create emitting structures on commercial 1-cm-diam borosilicate filter disks (Duran Group, Inc., P5 grade). This method is not well suited for fabricating two-dimensional (2-D) arrays of small emitters, as the pitch would be limited to the end-mill diameter. Instead, we have targeted linear emitter strips comprising triangular prisms $\sim 350 \mu\text{m}$ tall, 7 mm long, and having a half-angle of 30 deg. The apex radius of curvature is not controlled but must, at least, be larger than the particles within the porous glass, typically a few micrometers. In the demonstration devices presented here, nine emitter strips are fabricated per disk, spaced 0.8 mm apart. The milling process is detailed in Sec. III and has been developed exclusively for forming porous glass structures. However, porous metal structures of similar geometry could warrant investigation if the risk of pore sealing during milling was well managed or suppressed.

As indicated in the figure, we anticipate numerous emission sites to form along the sharp edge of each emitter strip. These emission sites are expected to form somewhat randomly, wherever local electric fields, pore loci, and hydraulic interactions permit. A first, empirical approximation as to the number of anticipated emission sites can be made through considering [24]. There, porous nickel emitters were positioned roughly 50 to 210 μm below a solid stainless-steel plate, which served as both an extractor electrode and a simple target. After operating for tens of minutes, numerous distinct impressions were observed on the plate and clustered around the positions of individual emitters. The impressions were assumed to be indicative of individual emission sites. Of particular relevance, when using axisymmetric emitter structures terminated by a flat plateau rather than a sharp

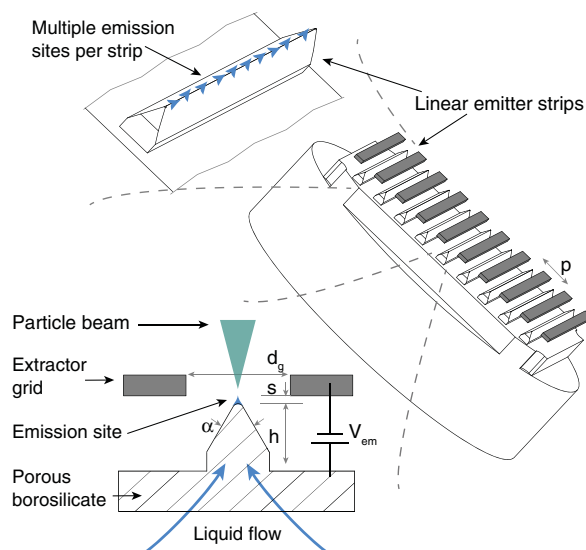


Fig. 1 Emitter strips comprising triangular prisms have been formed by milling borosilicate glass.

point, numerous impressions were recorded in an often circular pattern. That observation particularly supported the notion of multiple emission sites forming from pores near the strongest electric field. In that experiment, plateau perimeters were on the order of 100 μm . Inferring that a few emission sites can therefore be sustained per 100 μm of length, we anticipate that ~ 500 or more emission sites may be feasible from the presented devices considering the total edge length of 63 mm, although the materials and electrostatic configurations differ significantly.

II. Indirect Performance Calculations

Indirect thrust measurements have been calculated with an emphasis on TOF spectrometry, complemented and refined with beam angle and retarding potential analyzer (RPA) measurements. We first review the interpretation of the data acquired from each of these measurements in order to define corresponding propulsive parameters that enable functional thrust and mass flow rate calculations.

TOF measurements, where the current is recorded at a detector some known distance from a fast electrostatic gate, have been applied in numerous propulsion studies [5,19,21,22,30,31] throughout the development of electrospray thrusters. Delays between the gate signal and changes in the beam current detected indicate the flight time, and thereby speed, of constituent particles within the beam. The flight time t_ξ of particle ξ relates to its mass m_ξ and energy qV_a through Eq. (1):

$$t_\xi = L \sqrt{\frac{m_\xi}{2q|V_a|}} \quad (1)$$

In so far as the beam is assumed to be monoenergetic, with accelerating potential V_a , the distribution of current over flight time thus equivalently provides a distribution over the mass-to-charge ratio m_ξ/q . The thrust and mass flow rate due to the collected species can be calculated through appropriate integrals of the TOF trace [19]:

$$T_{\text{TOF}} = -\frac{2|V_a|}{L} \int_0^\infty F_T(t) t \frac{dI(t)}{dt} dt \quad (2)$$

$$\dot{m} = -\frac{2V_a}{L^2} \int_0^\infty F_m(t) t^2 \frac{dI(t)}{dt} dt \quad (3)$$

Here, T_{TOF} refers to the thrust as derived from TOF data and serves as the foundation for ITMs in this paper. L is the TOF flight tube length, and $I(t)$ is the collected current as a function of flight time. The factors $F_T(t)$ and $F_m(t)$ are nondimensional modifiers to the TOF integrand added to account for solvated ions that fragment after emission but before complete acceleration [32].

We are focused on IL electrospray sources operating at or near the PIR (ILIS [7]). Emitted beams therefore primarily comprise ions of the form $[AB]_n A^+$ and $[AB]_n B^-$ in the positive and negative emission modes, respectively. Here, A^+ and B^- are the positive and negative constituent ions of the IL, respectively, and n indicates the degree of solvation. The PIR has typically referred to emissions comprising primarily $n = 0$ and $n = 1$ ions, a small population of $n = 2$ ions, and no significant current with $n > \sim 4$ [7,16,33].

The ion population may fragment significantly in the field-free regions between the source and TOF detector. However, these fragmentation events do not alter performance and the fragmented ions are not expected to possess a significantly different speed than the parent. Hence, in the context of the Faraday cup-type detector used in this study, the speed of those detected ions alone can be interpreted to calculate the original parent mass. Conversely, ions that fragment between the emitter and extractor electrodes accelerate to a greater speed than the parent ion, and therefore have a lower flight time. Without adjustment, TOF-based calculations attribute intermediate masses to these ions assuming the complete energy qV_a , whereas in actuality, signals at interior flight times are indicative of two emitted particles, each with energy less than qV_a : an ion of mass

m_i and a neutral particle of mass m_N , which is otherwise undetected. Courtney and Shea have shown in [32] that, if specific fragmentation transitions are assumed, $F_T(t)$ and $F_m(t)$ can be simply calculated using Eqs. (4) and (5), respectively:

$$F_T(t) = \frac{K_i(t)}{qV_a} + \left(\frac{m_N K_n(t) K_i(t)}{m_i q^2 V_a^2} \right)^{1/2} \quad (4)$$

$$F_m(t) = \left(1 + \frac{m_N}{m_i} \right) \frac{K_i(t)}{qV_a} \quad (5)$$

Energy measurements of ILIS beams have indicated that fragmentation events from solvation n to $n - 1$ are dominant [34]. Neglecting other transitions, the ion and neutral fractional kinetic energies are then simply related to the flight time as the functions $K_i(t)/qV_a = t_{n-1}^2/t^2$ and $K_n(t)/qV_a = 1 - t_{n-1}^2/t^2$, respectively. Here, t_{n-1} refers to the ion flight time after breakup and the expressions are piecewise functions for each region $t_{n-1} < t < t_n$. In Sec. V, we find that the effects of these adjustments on aggregate calculations are small (a few percent) yet not negligible.

It is convenient to isolate the influence of distributed m_ξ/q , which is the primary output of the TOF, from the emission current and accelerating voltage in Eqs. (2) and (3). In this study, we consider two ionic liquids: 1-ethyl-3-methylimidazolium-bis(trifluoromethylsulfonyl)imide (EMI-Im) and 1-ethyl-3-methylimidazolium-tetrafluoroborate (EMI-BF₄). As the EMI⁺ ion is common to both liquids, we define a nondimensional flight time \bar{t} such that $t = t_{\text{EMI}} \bar{t}$, where t_{EMI} is the flight time expected by Eq. (1) for an ion of mass $m_{\text{EMI}} = 111.2$ Da. Furthermore, we define a nondimensional current \bar{I} such that $I(t) = I_c \bar{I}(\bar{t})$, where I_c is the current collected in the absence of a gate. It then follows that

$$T_{\text{TOF}} = \kappa \sqrt{\frac{2m_{\text{EMI}}}{q}} I_c \sqrt{|V_a|} \quad (6)$$

$$\dot{m} = \phi \frac{m_{\text{EMI}}}{q} I_c \quad (7)$$

$$\kappa = - \int_0^\infty F_T(\bar{t}) \bar{t} \frac{d\bar{I}(\bar{t})}{d\bar{t}} d\bar{t} \quad (8)$$

$$\phi = - \int_0^\infty F_m(\bar{t}) \bar{t}^2 \frac{d\bar{I}(\bar{t})}{d\bar{t}} d\bar{t} \quad (9)$$

The parameters κ and ϕ are nondimensional coefficients relating thrust and mass flow rate, respectively, to the same metrics if the beam were attributed solely to particles of mass m_{EMI} at the same current and voltage. Recognizing that $-d\bar{I}(\bar{t})/d\bar{t}$ is a normalized distribution of current versus flight time and, by Eq. (1), that t is proportional to $\sqrt{m_\xi/q}$, we may alternatively view κ and ϕ as providing relative measures of the means $\sqrt{m_\xi/q}$ and m_ξ/q , respectively. Ultimately, these nondimensional parameters enable a quantitative view to the consistency in beam composition, as relevant to propulsive performance, decoupled from voltage and current.

In applying Eq. (7) to estimate total mass flow, we have assumed an average of ϕ over beam angle and emitter voltage, and therefore replace the TOF detector current I_c with the total emitted current I_{em} .

To calculate total thrust, consideration must be made for the spread of beam angles with respect to the thruster normal. Depending on the source type and measurement definition, the ILIS beam half-angles may range from ~ 15 [7] to 40 deg [35]. To maintain relevance to

propulsive parameters, we define a beam angle parameter based on thrust rather than current inclusion. Consider probe measurements at an angle θ to the thruster normal. Referring to Eq. (6), the thrust contribution due to an element of collected current $dI_c = j dA$ is

$$dT(\theta) = \kappa \sqrt{\frac{2m_{\text{EMI}}}{q}} \sqrt{|V_a|} j(\theta) \cos \theta dA \quad (10)$$

Here, j is the current density at the sample angle θ , and dA refers to an elemental area at the probe collection point some L_c from the source. Note that κ and V_a may vary over angle; however (see Sec. VI. D), we have observed these quantities to remain reasonably stable from our sources, and hence consider them to be constant. The total thrust can then be estimated through integration of Eq. (10) over a surface S enclosing the beam. Normalizing by the total beam current I_b such that $j = jI_b$ and integrating, we obtain

$$T = \kappa \sqrt{\frac{2m_{\text{EMI}}}{q}} I_b \sqrt{|V_a|} \cos \theta_{\text{eff}} \quad (11)$$

$$\cos \theta_{\text{eff}} = \int_S \bar{j}(\theta) \cos \theta dA \approx \pi L_c^2 \int_0^{\theta_{\text{max}}} \bar{j}(\theta) \sin 2\theta d\theta \quad (12)$$

Intrinsically, in Eq. (11), it has been assumed that the complete beam current I_b has been sampled, such that the surface integral of \bar{j} is unity. The angle θ_{eff} is the angle of a hollow emission cone yielding the same thrust as the device under test. The approximation on the right side of Eq. (12) assumes an axisymmetric beam of extent θ_{max} and is the form ultimately applied here. In Sec. V, an offset angle θ_0 has also been calculated, permitting axisymmetric beam approximations about an axis tilted with respect to the thruster.

The accelerating voltage V_a will generally differ from the applied emitter voltage V_{em} by some deficit ΔV . Reported values of ΔV range from a few volts [34,36] to more than 100 V [4], depending on the source and operating conditions. Energy deficits may include intrinsic physical mechanisms, such as the ion solvation energy and ohmic losses at the Taylor cone apex, or external influences, such as series resistances upstream of the electrical path. Some such losses may not be constant over species mass [37]. In this study, the impact of such variability was small, and average fractional energy deficits were assumed for the entire spectrum. These deficits have been determined via both TOF and RPA measurements; see Sec. V.

Finally, it is important to acknowledge that the beam current contributing to thrust I_b may be lower than the measured emitter current I_{em} due to interception at the extraction grid I_{ex} such that $I_b = I_{\text{em}} - I_{\text{ex}}$.

Considering the accumulated factors described, in Eq. (13), we relate the expected thrust to the readily measurable extractor voltage and beam current along and with the known mass m_{EMI} . The specific impulse and propulsive efficiency in Eqs. (14) and (15), respectively, then follow, with the mass flow determined by Eq. (7) with I_c set to I_{em} :

$$T = \kappa \sqrt{\frac{V_a}{V_{\text{em}}}} \cos \theta_{\text{eff}} \left[\sqrt{\frac{2m_{\text{EMI}}}{q}} I_b \sqrt{|V_{\text{em}}|} \right] \quad (13)$$

$$I_{\text{sp}} = \frac{T}{\dot{m}} = \frac{\kappa}{\phi} \frac{I_b}{I_{\text{em}}} \sqrt{\frac{V_a}{V_{\text{em}}}} \cos \theta_{\text{eff}} \left[\frac{1}{g} \sqrt{\frac{2q|V_{\text{em}}|}{m_{\text{EMI}}}} \right] \quad (14)$$

$$\eta_{\text{prop.}} = \frac{T^2}{2\dot{m}I_{\text{em}}V_{\text{em}}} = \left(\frac{I_b}{I_{\text{em}}} \right)^2 \frac{V_a}{V_{\text{em}}} \frac{\kappa^2}{\phi} \cos^2 \theta_{\text{eff}} \quad (15)$$

The specific impulse I_{sp} is expressed as that which would result from pure EMI emission at the emitter voltage magnitude (in square brackets) modified by parameters due to the mass distribution, beam interception at the grid, energy deficits, and angular spreading. Typical high-current, passively fed, IL electrospray sources operate with $V_{\text{em}} \sim 1\text{--}2$ kV [2,5,22], corresponding to an idealized specific impulse of $\sim 4000\text{--}6000$ s for particles of mass m_{EMI} . However, we demonstrate in this paper that lower values, $\sim 1000\text{--}3000$ s, may result once all the listed parameters and both emission polarities are considered.

The constituent terms contributing to propulsive efficiency $\eta_{\text{prop.}}$ in Eq. (15) are largely analogous with those considered in other electrostatic propulsion systems (e.g., [38]) and are discussed in greater detail in [39,34]. The terms V_a/V_{em} and $\cos^2 \theta_{\text{eff}}$ are easily recognized as extraction energy and angular losses respectively, whereas $(I_b/I_{\text{em}})^2$, which is a form of utilization efficiency, arises due to the loss of propellant and expended energy associated with accelerated particles striking the extractor grid. The quantity κ^2/ϕ is of particular importance for electrospray thrusters [19]. Referred to as the “polydisperse efficiency” [8], it provides a measure of the apparent power loss associated with the emission of a disperse beam, with respect to charge-to-mass ratios. Low polydisperse efficiencies (less than 50%) can result from only a few percent of large droplets within an otherwise ionic beam [40], greatly penalizing the power efficiency when targeting a high specific impulse through the PIR. This relatively severe loss mechanism has led to significant focus on achieving the PIR [26,41] or, more recently and with promising results, obtaining extremely small (\sim few kDa) monodisperse droplet beams [20]. In this regard, ILISs that achieve the PIR through externally wetted [7] or porous [16] electrospray emitters are a promising avenue for high-efficiency high-specific-impulse devices. Indeed, in [8], a relation similar to Eq. (15) was derived and used to motivate that total propulsive efficiencies approaching 90% may be achievable through ILISs emitting EMI-BF₄. In Sec. VI, we compare the thrust calculated as per Eq. (11) with direct thrust measurements and apply Eqs. (14) and (15) to estimate the specific impulse and propulsive efficiencies of three demonstration devices.

III. Source Preparation

Three devices have been fabricated and tested: two wet with the IL EMI-Im, and a third wet with EMI-BF₄. These liquids were selected due to existing heritage with ILISs in the literature (for example, see [34,37] and [7] for studies of EMI-Im and EMI-BF₄, respectively). Furthermore, the heavier negative ion mass of Im[−] (280.2 Da) versus BF₄[−] (86.8 Da) and possibility of droplet (or at least very large n) emissions [37] were expected to yield higher thrusts at the expense of polydisperse efficiency. The two EMI-Im and single EMI-BF₄ sources are hereafter referred to as SRC-Im-1, SRC-Im-2 and SRC-BF₄, respectively.

A. Fabrication Process

The Duran Group, Inc., P5 grade 1-cm-diam 3-mm-thick porous filter disks were machined using a small tabletop CNC mill (Step-Four Basic 540). The forming process is outlined in Fig. 2, where dark (shaded) regions indicate material to be removed at each step. The process comprises the following steps:

- 1) A square profile is defined to facilitate mounting.
- 2) A clear out region and slight chamfer are defined to provide a buffer between the mounting flange and emitter strips.
- 3) The sample is rotated by 30 deg with respect to the vertical, and nine cuts are made.
- 4) The sample is rotated to -30 deg with respect to the vertical, and offset strips are cut to fully define the emission edges.
- 5) Finally, the material between and beyond each emitter strip is removed to expose triangular prisms.

Steps 1 and 2 through 5 are made with 2- and 0.5-mm-diam Titanium aluminum nitride (TiAlN)-coated end mills, respectively. Due to the abrasive nature of borosilicates, a new 0.5 mm bit was required for each device. Figures 3 and 4 present photographs and a multifocal microscope image of the source emitters used in this study.

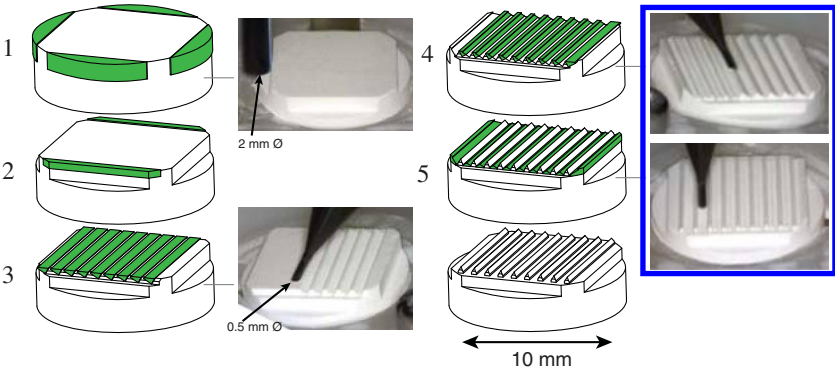


Fig. 2 Emission source machining process. Shaded segments are removed at each step.

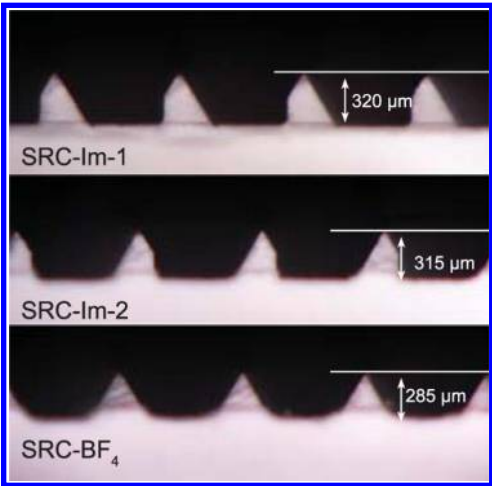


Fig. 3 Side profiles of the three devices used in this test after CNC machining. Alignment errors between steps 4 and 5 in Fig. 2 lead to the asymmetric shapes visible in SRC-Im-1 and SRC-Im-2.

The multifocal image in Fig. 4 demonstrates that, while low radii-of-curvature of a few tens of micrometers are achievable with the method, an undulated ridge with a range of apex radii was typical. The asymmetric profiles in Fig. 3 for devices SRC-Im-1 and SRC-Im-2 are evidence of inaccuracies in the milling reference point between rotated configurations. However, relative to the apex radius, these asymmetries lie far from the anticipated emission site loci and the influence is not expected to be large. Generally, these inconsistencies in fabrication may be regarded as a clear shortfall when compared with the precision achievable from silicon microfabrication [17,21,26]; however, the tip curvature ranges are comparable with other porous sources [5,16,27].

B. Final Assembly and Wetting

The demonstration thruster assembly used in this study is summarized in Fig. 5. Each emitter layer was stacked with a second porous

borosilicate reservoir layer of larger $\sim 16 - 40 \mu\text{m}$ pores (Duran Group, Inc., P3 grade). These two layers were interfaced using a laser-cut disk of Whatman qualitative number 1 filter paper, ensuring a continuous porous path between both layers. The emitter layer was supported within a polyether ether ketone (PEEK) mount by means of an aluminum guard ring. This flange served two additional purposes:

- 1) It was used as the electrical contact point with the IL.
- 2) The guard ring suppressed the electric field strength at the edges of the disk, preventing spurious emissions into the extractor grid.

The PEEK upper and lower mounts, and thereby the two porous disks, were then retained in contact with a mild pressure via springs. External electrical contacts to the emitter layer, via the guard ring, and the extractor grid were achieved through Pogo™ pins soldered to a small circuit board mounted on the top of the assembly. Each device was wet with IL in a two-part process before alignment and bonding with an extractor grid. First, $90 \mu\text{L}$ of ionic liquid, which had been previously degassed for at least 1 h under a less than 10^{-5} mbar vacuum, was added to the front of the device to completely fill the emitter layer. The assembly was then placed under vacuum for an additional 2 h to promote filling. Finally, an additional 20 to $30 \mu\text{L}$ was added to the emitter surface in order to ensure complete saturation of the emitting layer with all excess liquid retained by the reservoir and interface layers. Liquid transport during operation was entirely passive; no external flow connections or feeding mechanisms were present.

The extractor grids comprised $350\text{-}\mu\text{m}$ -wide 9-mm -long channels laser cut from sheets of $100\text{-}\mu\text{m}$ -thick molybdenum. The grids were aligned using an optical microscope and held in place using layers of double-sided Kapton® tape. This grid placement method resulted

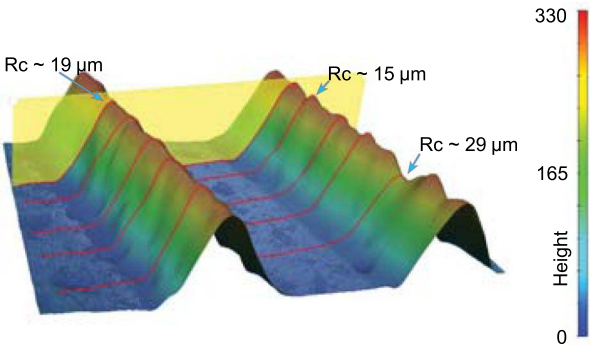


Fig. 4 Multifocal microscopic image of SRC-Im-2 indicating the typical degree of apex undulation resulting from the milling process.

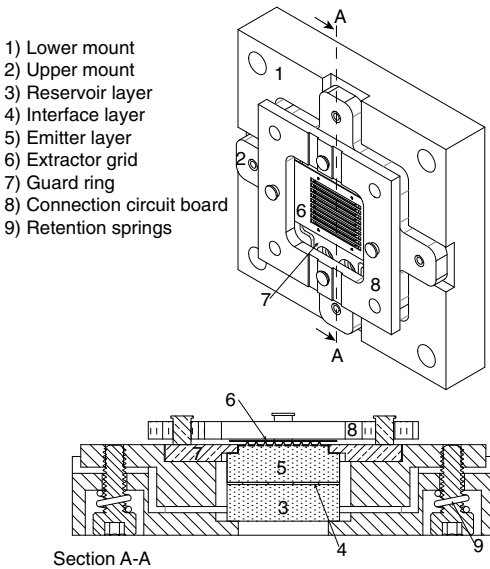


Fig. 5 Constituent components of the demonstration thrusters tested here.

in a degree of variability in the grid position between devices. Horizontally, the alignment was typically within a few tens of micrometers of the strip center along the length of emitter strip. However, the spacing between emitters and the grid, which is a relatively pertinent dimension in the context of the electric field at a given voltage, varied by tens of micrometers; see Table 1. In the table, s is the distance between the emitter edge and the base of the extractor, as indicated in Fig. 1. This preliminary design targeted a separation s of zero, such that the emitting edge and extractor plate were in line, in an effort to ensure moderate starting potentials and low grid interception. However, referring to the table, the emitting edges tended to protrude into, but not through, the extractor grid for both sources emitting EMI-Im and were $150\ \mu\text{m}$ below the extractor on average for SRC-BF₄.

The minimum voltage to start emission can be estimated through recognizing that the applied electrostatic pressure must overcome the liquid surface tension [38,42] and, particularly relevant in porous devices [2], the negative Laplace pressure due to the porous reservoir. The cited relations indicate a minimum voltage that scales with the liquid surface tension γ and length scales f and r_p for the emitter field enhancement and capillarity length scales, respectively; $V_{\text{start}} \sim f\sqrt{\pi\gamma/2r_p}$ [42]. Given the transverse undulations and range of curvature radii resulting from this process, and the potential for augmented field enhancement due to the liquid shape within the dielectric structure [29], accurate predictions by this relation were not expected. Nonetheless, 2-D (planar) finite element method (FEM) simulations of the electric field were used to predict f for a $20\ \mu\text{m}$ representative radius of curvature and the grid separations/emitter heights listed in Table 1. As indicated, emissions were broadly anticipated to initiate in the vicinity of 1550 and 2100 V for the devices wet with EMI-Im and EMI-BF₄, respectively. The surface tension values listed in Table 1 and used to estimate V_{start} are from Ref. [43].

The assembled devices measured $3.7 \times 3.7 \times 0.8\ \text{cm}$ and, once wet, had a typical mass of $\sim 16\ \text{g}$. With IL retained by the porous reservoir, the devices could be easily handled and transported once wet, permitting tests at multiple facilities without disturbing the liquid state. The outer device dimensions could be reduced in the future to more efficiently enclose the $\sim 1\ \text{cm}^2$ of emitting area. In particular, it should be noted that the PEEK mounting structure represented 10 g of the total mass and the design favored accommodation within the test facilities over size.

IV. Experimental Apparatus and Methods

Measurements were acquired at both the ESA Propulsion Laboratory (EPL) within the European Space Research and Technology Centre (ESTEC) in Noordwijk, The Netherlands, and the Microsystems for Space Technologies Laboratory (LMTS) at École Polytechnique Fédérale de Lausanne (EPFL). Direct thrust measurements were made first, at ESTEC, followed by probe measurements at the LMTS.

A. Direct Thrust Measurement

The low mass and lack of fluidic connections made the demonstration thrusters suitable for DTMs via a precision commercial mass balance modified for use within a vacuum facility. At the ESTEC EPL, A Mettler Toledo XP2004-S balance was installed within a 0.8-m-diam 0.5-m-tall cylindrical facility pumped by a Pfeiffer TMH 261 turbomolecular pump with a Pfeiffer MVP 055-3 diaphragm forepump. With all components installed, including the wetted thruster,

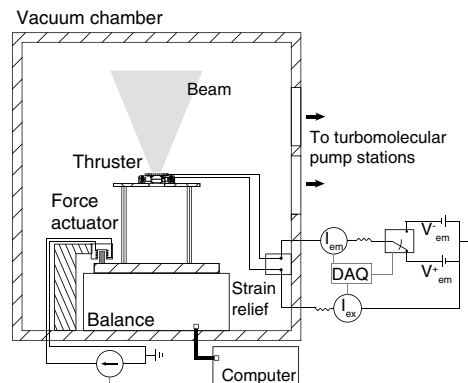


Fig. 6 ESTEC test configuration. The thruster was positioned to emit upward.

the base pressure was $\sim 3 \times 10^{-6}$ mbar; however, during operation at the highest currents observed for SRC-Im-1, the recorded pressure surged to up to 9×10^{-5} mbar. Before testing SRC-Im-2 and SRC-BF₄, an additional TMH 261 turbopump station was added in parallel to improve the extraction rate. The peak pressure was subsequently less than 6×10^{-5} mbar when emitting.

The thrusters were positioned as indicated in Fig. 6, and mounted to emit upward. Propellant wetting was performed, as described in Sec. III.B, before installation in the facility. Hence, only the emitter and extractor electrical connections were required: no fluid lines were present. The connections to high-voltage vacuum feedthroughs were made via a strain relief block to reduce disturbances. The emitter voltage was supplied via FuG Elektronik HCN 140-12500 and HCN 35M-20000 high-voltage power supplies for the positive and negative states, respectively. The emitter polarity was controlled via a custom switching box controlled via a National Instruments USB-DAQ (USB Data acquisition board).

The emitted and extractor (intercepted) currents were measured with optically isolated current monitors, accurate to within ~ 3 and $2\ \mu\text{A}$ for the emitter and extractor monitors, respectively. As shown explicitly in Fig. 6, each monitor included an inline high-power $100\ \text{k}\Omega$ resistor along the current path to protect the monitors against short circuits. The voltage drop along these resistors was calculated and accounted for in all data presented. That is, reported energy deficits ΔV were in excess of this known ohmic drop.

The balance specified repeatability was $\sim 1\ \mu\text{N}$ ($0.1\ \text{mg}$). In practice (see Sec. V), the standard deviation in balance output was typically $\sim 2\text{--}3\ \mu\text{N}$ with very low-frequency (tens to hundreds of millihertz) random undulations of similar order. The balance stability was therefore a significant source of measurement uncertainty during direct thrust measurements. Each thrust measurement consisted of the difference between an average over at least 30 s of thruster operation and the average of 30 s measurements preceding and following the measurement. The first 7 s of thruster activity were discarded to allow the balance and beam emissions to settle.

The balance consistency was evaluated periodically throughout the test using an electromagnetic force actuator. Here, a Keithley 2440 SourceMeter was used to drive prescribed currents through a coil to impart a consistent force, from 10 to $1000\ \mu\text{N}$, while monitoring the balance output. Beginning with the unloaded balance in atmosphere, the slope of the balance output versus driving current and the drift over an $\sim 20\ \text{min}$ period were recorded sequentially as a dry thruster was installed, the chamber was evacuated, and finally, high voltage (1500 V) was applied. Once a stable configuration was reached, the sensitivity curve remained constant to within the standard error ($\sim 2\%$), whereas the change in averaged (over 30 s) output was typically $< 5\ \mu\text{N}$ over the $\sim 20\ \text{min}$ process. This feedback consistency was confirmed to persist before and after each thruster test.

Emissions from ILISs are known to decay over time [44], particularly at constant emitter polarity. These reductions can, in part, be attributed to electrochemical breakdown of IL at the liquid-conductor interface [45]. To suppress these reactions, the potential

Table 1 Device dimensions and ionic liquid properties

Device	$h \pm \sim 20\ \mu\text{m}$	$s, \mu\text{m}$	$\gamma, \text{mN/m}$ [43]	$V_{\text{start}}^a, \text{V at } R_c = 20\ \mu\text{m}$
SRC-Im-1	320	-20 ± 20	34.9	~ 1550
SRC-Im-2	315	-50 ± 35	34.9	~ 1550
SRC-BF ₄	285	105 ± 30	45.2	~ 2100

^aPredicted.

Table 2 Direct thrust measurement setpoints

Device identification	κ^+/κ^-	α , %
SRC-Im-1	0.53	34–36
SRC-Im-2	0.77	43–45
SRC-BF ₄	1.0	50

is typically alternated to prevent sufficient charge accumulation at the interface for charge transfer to occur [33,44]. Further work has indicated the efficacy of this method may be augmented when using a distal electrode [46], which is a scheme intrinsically implemented when using porous glass emitters, as done here. The efficacy of potential alternation alone has been debated, indicating that, at least, efforts should be made to balance the total charge emissions over each period [33].

In the context of our goal of comparing direct and indirect thrust measurements, potential alternation represents an added complexity due to the possible imbalance of thrust levels between polarities. Preliminary attempts to measure thrust in a unipolar (no alternation) configuration were unreliable, as the emission current tended to decay dramatically, by over 40% at times, and did not tend to fully recover even after subsequent operation with alternation (in contrast to [37]). Hence, a potential alternation scheme has been adopted. In keeping with the literature, and in lieu of accurate knowledge of the liquid-metal contact area of our device, the potential was alternated at 1 Hz during thrust measurements. Considering the few seconds of response time and high-amplitude noise inherent with the balance, resolution of the thrust within each period was not possible. To reduce effects due to the unknown balance response when subjected to a pulsed thrust, the emitter voltage in each polarity was selected in an attempt to achieve equal thrusts at any moment. The alternation duty cycle α was then selected to target balanced total charge emission over each period.

Referring to Eq. (13), in so far as beam spreading and fractional energy deficit may be approximated as constant, the thrust from each polarity will be proportional to $\kappa|I_b|\sqrt{|V_{em}|}$. Despite decays, a few (~ 10) constant voltage thrust measurements were made for each device so as to estimate the ratio of proportionality factors κ between polarities: κ^+/κ^- . These ratios are indicated in Table 2 and are discussed, with the hindsight of the subsequent indirect thrust measurements in Sec. VI. Measurements of current versus voltage, while alternating the potential, were then used to predict the expected current imbalance at equal thrusts, thereby enabling selection of the duty cycle such that $\alpha I_{em}^+ + (1 - \alpha)I_{em}^- \approx 0$. For device SRC-BF₄, the predicted ratio of thrusts and measured current-voltage curves corresponded to well-matched positive and negative outputs, leading to selection of simply matched voltages and a 50% duty cycle. This result is in keeping with previous studies where voltage alternation alone, without other means to ensure balanced charge, was shown to suppress electrochemical reactions with EMI-BF₄ [44].

B. Indirect Thrust Measurement

The LMTS facility consists of a six-way ISO160 cross combined with an 0.8 m ISO100 extension serving as the flight tube and evacuated by a Varian V70 turbomolecular pump. The base pressure was less than 3×10^{-6} mbar, rising to $\sim 6 \times 10^{-6}$ mbar when the emission spray was active. Figure 7 provides an overview of facility as configured for TOF and beam angle measurements.

Emitter and extractor currents were monitored using the same optically isolated transducers used at ESTEC. Similarly, the emission polarity was alternated using the aforementioned switching box, now controlled via an Agilent 33220a arbitrary function generator. Stanford Research Systems P350 high-voltage power supplies were used to control the electrostatic gate potential along with the positive and negative emitter currents.

The TOF spectrometer was positioned 13 cm from the source and comprised a gate assembly, flight tube, and detector assembly. The flight distance from the gate electrode to the detector assembly was 74.6 cm. The detector assembly comprised two 81% transparency

stainless-steel meshes upstream of a stainless-steel plate, with the central mesh biased to -40 V to suppress secondary electron emission from the detector plate. The detection area was 11.3 cm^2 .

The electrostatic gate consisted of three 81% transparency stainless-steel planar meshes. The outer mesh electrodes were held at ground while the inner electrode was switched from ± 3000 V to ground at 25 Hz using a fast PVX-4140 high-voltage switch. The detector current was converted to a voltage using a FEMTO DHCPA-100 high-current amplifier, set to a gain of 10^6 V/A and 1 MHz bandwidth. The amplified output was recorded on a LeCroy WaveSurfer 424 digital oscilloscope with ~ 30 trace averaging enabled to improve the recorded signal-to-noise ratio.

The TOF flight tube was accessed through a 6.3-mm-diam aperture, corresponding to a narrow ± 1.4 deg acceptance angle. Despite the clear drawback of reduced signal intensity, the narrow acceptance angle had two benefits. Primarily, we have observed that, at the hundreds of microampere beam currents typical from these devices, secondary electron emission from impinging surfaces within the flight tube can become a major source of error. Spurious current signals, at times including offset currents of comparable order to the primary signal, were typical until access to the flight tube was restricted. The aperture geometry was selected such that, geometrically, all particles passing into the TOF flight tube would reach the detector; that is, none were anticipated to strike the inner walls of the TOF tube upstream nor beside the collector assembly. As part of a larger baffle structure, the aperture also inhibited secondary electrons born near the flight tube entrance from reaching the high-voltage gate electrode. With this system, and the aforementioned -40 V screen grid upstream of the detector in place, relatively clean TOF traces with low (few nanoamperes) offsets were achieved.

The thrusters were mounted on a manual rotation stage, enabling angle resolved beam current and TOF measurements over ± 50 deg about the central emitter strip. Beam profiles over the angle were made using the TOF assembly detector with the gate electrode held to ground. The narrow acceptance angle of the TOF flight tube reduced corruption of the data due to the finite extent of the sources. Specifically, referring to Eq. (12), we seek an effective angle representative of all beamlets, regardless of their spatial distribution within the plane of emitting structures. The spatial spread due to long slits could present system challenges in managing the exhaust plume, but it would not alter the thrust output in so far as all beamlets are considered equal. Using the aperture configuration described, the detected current contributions due to a beamlet located at the maximum extent from the center of the thruster (~ 4.7 mm) were within ~ 1 deg of the stage angle. However, the collection solid angle for such a beamlet, as estimated using simulations with the commercial software Simion 8.1, was significantly reduced compared to emissions from the center of the device. Referring to Sec. II, integration of the measured current density versus angle should correspond to complete collection of the emitted beam. However, we have calculated through the aforementioned simulations that no more than 60% and as little as 40% of the emitted beam may be detected due

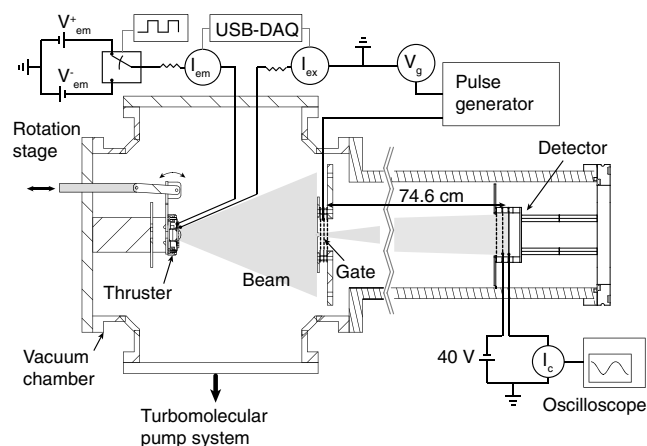


Fig. 7 Schematic of the test configuration used at LMTS as configured for TOF measurements.

to the reduction in transmission for distributed beamlets. It is important to clarify that this reduction is geometric and should not, in so far as emission characteristics are uniform over the source, correspond to a possible ambiguity in interpreting the TOF spectra.

TOF and beam angle measurements have been complimented by limited retarding potential analyzer measurements. The RPA primarily consisted of seven stainless-steel mesh grid electrodes in line with a Kimball Physics FC-72 Faraday cup detector. In keeping with previous high-resolution energy measurements from ILISs [34,36], the RPA design was based on the recommendations of [47]. Specifically, to ensure smooth potential gradients, the retarding potential was distributed over five grids, wherein the three central grids were at the retarding potential V_r , whereas the outer grids were maintained at 96% of V_r . A 9.5-mm-diam limiting aperture on the RPA's Faraday cup collector was positioned 71 mm from the source.

V. Results

A. Direct Thrust Measurements

Emitted currents I_{em} versus the applied voltage $|V_{em}|$ (I-V data) for each of the tested devices are shown in Figs. 8 and 9. All three devices were shown to emit several hundred microamperes at potentials consistent with the rough starting potential estimates in Table 1. These data were acquired with the potential polarity alternating at 1 Hz and with a 50% duty cycle. Each datum represents the mean and standard deviation (error bars) of data collected at each polarity over a 3 s period. Short transients when switching polarity were discarded. The figure insets provide representative snapshots of the raw emitted current measured at one setpoint. For both devices operated with EMI-Im, negative emission currents tended to increase gradually across each half-period for all devices, contributing to the larger standard deviations indicated in the primary figures. These I-V relationships were applied to establish the duty-cycle setpoints in Table 2 necessary to approach balanced total charge emission in tandem with equal positive and negative thrusts.

Typically, a few percent of the beam was intercepted by the extraction grid, as indicated by I_{ex} in the figures. Interception was greatest for SRC-Im-2 (Fig. 8b), where up to 10% of the beam was intercepted. These data are representative of the current-voltage behavior immediately before the DTMs. However, irreversible changes in the emission and interception currents did occur. In particular, the emission current tended to decrease gradually over the test campaign, particularly after returning to LMTS, whereas the current intercepted

by the grid tended to decrease. The decays are discussed in more detail in Sec. VI.C.

Raw current data and the accompanying thrust output acquired during a typical thrust measurement are shown in Fig. 10, from SRC-Im-1. Figure 10a demonstrates how lower current yet longer pulses per period in the negative mode were applied as per the open-loop thrust and current balancing scheme. The emission current clearly decayed throughout each thrust measurement, predominantly over the first few seconds. Horizontal lines indicate the region, after a 7 s delay, sampled to generate representative average positive and negative currents (solid lines) and standard deviations (dashed lines) for the measurement.

In Fig. 10b, the emitter supply was off before and after measuring thrust, providing reference zero levels. This example demonstrates both the few micronewton instabilities typical at short (few seconds) timescales along with a larger jump in the mean offstate output before and after emission. These pre- and postmeasurement zero levels were often in agreement; however, as in the presented example, a discrepancy approaching $\sim 5 \mu\text{N}$ was not uncommon. To arrive at a single measurement, the average balance output, after a 7 s settling period, was compared with the average balance output for 30 s before and 30 s after the pulse, as indicated in the figures. Solid and dashed lines

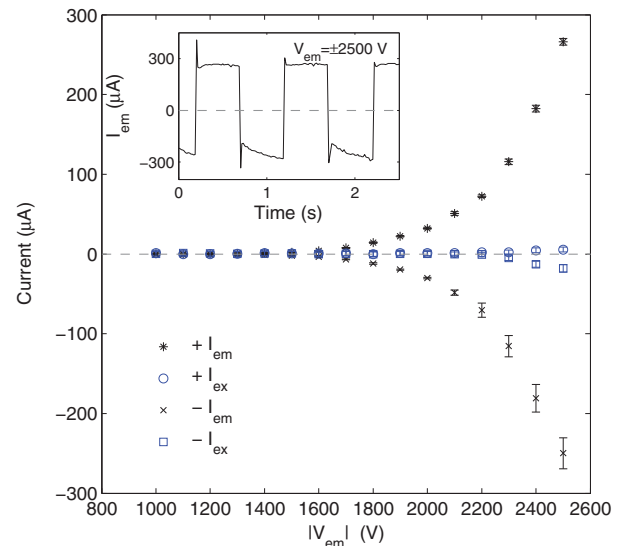
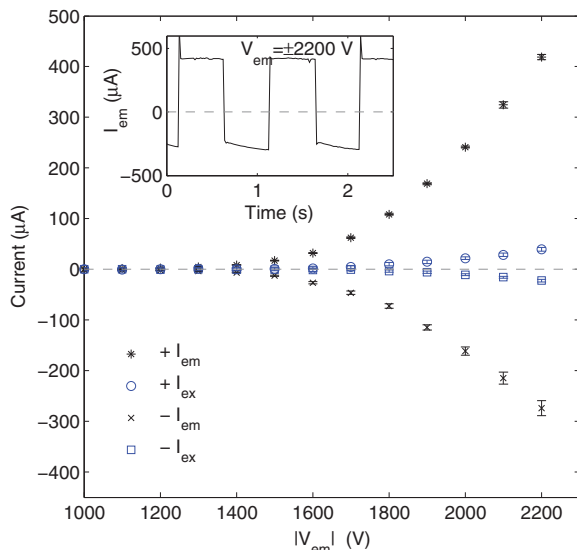
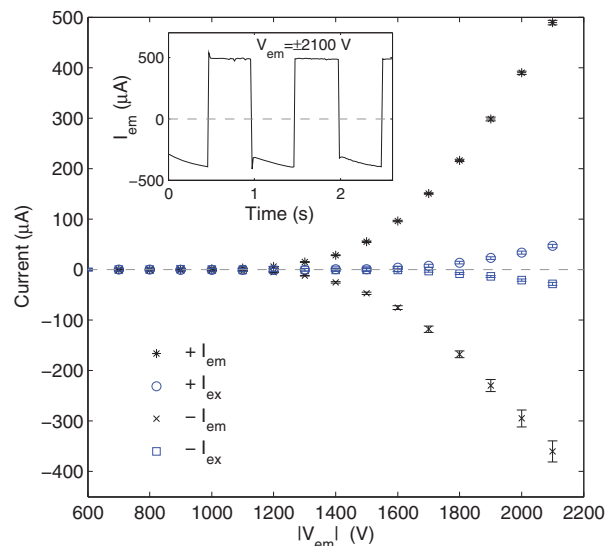


Fig. 9 Current versus voltage (I-V) characteristic for SRC-BF₄ immediately before direct thrust measurements.



a) SRC-Im-1



b) SRC-Im-2

Fig. 8 Current versus voltage (I-V) characteristics for the two sources emitting the IL EMI-Im immediately before direct thrust measurements.

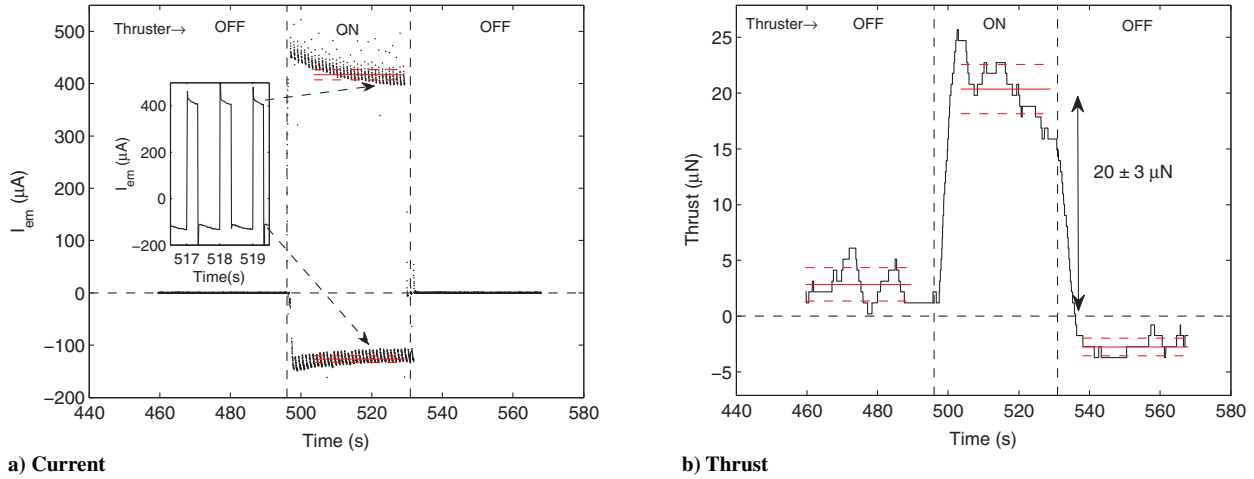


Fig. 10 Example of a typical current and corresponding thrust pulse from SRC-Im-1.

again represent the calculated means and standard deviations, respectively.

In Fig. 11, the thrust output from SRC-Im-2 has been plotted along with the quantity $\langle I_b \sqrt{|V_{em}|} \rangle = \alpha I_b^+ \sqrt{V_{em}^+} + (1 - \alpha) I_b^- \sqrt{|V_{em}^-|}$ recorded during each of a sequence of 10 repeated measurements at $V_{em} = +1997$ V / -2007 V. Despite the consistent emitter voltages, the beam current, and therefore $\langle I_b \sqrt{|V_{em}|} \rangle$, differed between repeated trials, tending to decrease. Accordingly and consistent with Eq. (13), the thrust also tended to decrease supporting correlation with this parameter; see the figure inset. In Sec. VI, we therefore compare all direct and indirect thrust measurements as a function of $\langle I_b \sqrt{|V_{em}|} \rangle$.

Scans of thrust measurements were made at setpoints interpolated, based on the I-V measurements, to yield 100 to 400 μ A of positive emitter current. Measurements at these setpoints were repeated several (3–10) times for each device, with the negative voltage and duty cycle established through Table 2. The summarized results, demonstrating tens of micronewtons at less than 1 W of power for all three devices, are presented later (Sec. VI) in comparison with the ITM.

B. Indirect Thrust Measurements

The three devices were transported from the ESA/ESTEC EPL facilities back to the LMST at EPFL for beam diagnostics. No modifications were made to any device, including to the liquid state. Specifically, no liquid was added or removed between tests. The devices were stored under vacuum whenever possible.

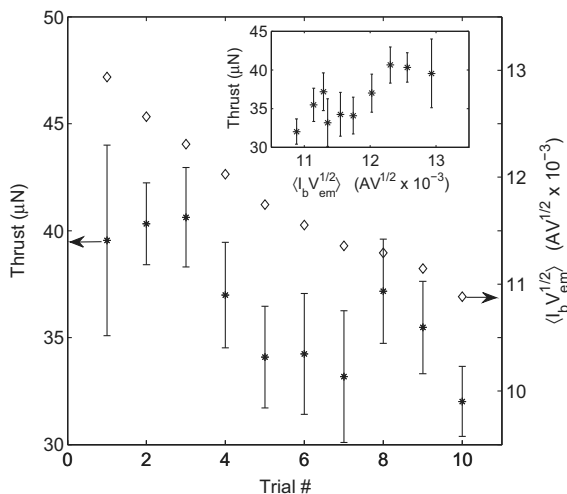


Fig. 11 Repeated thrust measurements at +1997/−2001 V and a 43% duty cycle from SRC-Im-2.

1. Time-of-Flight Spectrometry

TOF traces were acquired from each of the three test devices, forming a basis for propulsive metric calculations. As described previously, the measurement setup did not permit TOF measurements while simultaneously alternating the potential. Instead, all TOF measurements were made while emitting at constant polarity for several seconds.

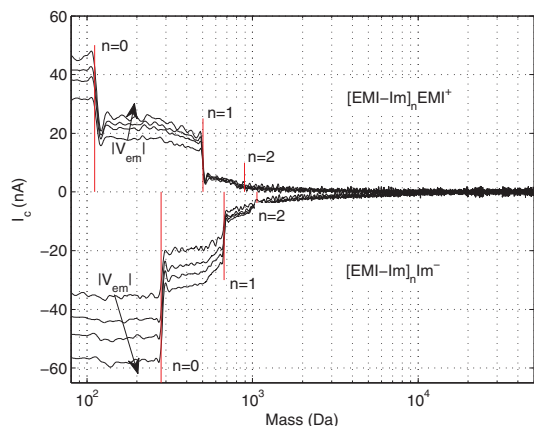
Each trace was postprocessed before determining the parameters κ and ϕ by Eqs. (8) and (9). First, the raw data were filtered using a Savitzky–Golay filter, as has been previously applied to TOF processing [20]. Any offset in output from the current amplifier, typically 1–2 nA, was then subtracted. Although modified by activating the source, this residual current was deemed spurious, as it was confirmed to persist over the full 20 ms half-period of the gate signal. Finally, the current trace was normalized by an average inlet current before the first species flight time.

The mean shift in beam energy between the measured and expected locations of ion peaks was determined through a Gaussian fit to the derivative of the trace near the ion flight times anticipated by Eq. (1) for the $n = 0$ and $n = 1$ species. The edge was then taken as being 0.22 μ s from each peak, corresponding to half the expected decay time of the amplifier from 95 to 5% at 1 MHz bandwidth. Voltage deficits ΔV_{TOF} for $n = 0$ and $n = 1$ species were taken as the difference between V_{em} , after correction for the inline sensing circuit resistance, and the equivalent voltage consistent with each edge by Eq. (1). The average of these two deficits was then taken to estimate V_a and used to calculate the flight time expected for ions of mass m_{EMI} , enabling a normalized \tilde{t} to be calculated and applied in Eqs. (8) and (9) for κ and ϕ , respectively.

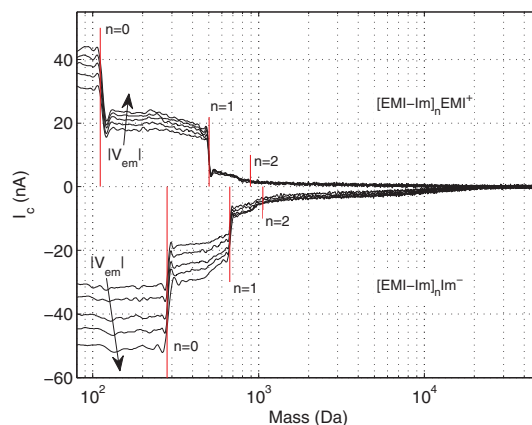
TOF measurements were made at ± 10 to 30 deg of rotation in addition to aligned 0 deg measurements. However, as detailed in Sec. VI.D, trends versus neither angle nor voltage were determined to a level of confidence clearly beyond the repeatability at consistent setpoints. Instead, the derived metrics presented here are an average over all measurement conditions (voltage, beam angle) per polarity.

Examples of TOF measurements for each device, at 0 deg rotation, are given in Figs. 12 through 13. The traces are presented as a function of the calculated species mass after correcting for energy deficits and assuming singularly charged ions. Vertical lines indicate locations of the known $n = 0$, $n = 1$, and $n = 2$ ion masses, showing good agreement in the first two cases. Highly ionic emissions were achieved in all cases, with most current corresponding to $n = 0$ and $n = 1$ species; however, a high n tail extending to several kDa was particularly evident at negative V_{em} from EMI-Im in Figs. 12a and 12b. The current contributions due to each ion species, taken as the change in fractional current between each calculated drop location, are given in Table 3.

Average voltage deficits for the $n = 0$ and $n = 1$ peaks are also provided in Table 3. In all instances, a higher ΔV was found for the $n = 0$ ion compared with $n = 1$, and lower deficits were observed at



a) SRC-Im-1: $|V_{em}|$ increasing from ± 2000 V to 2300 V in 100 V steps



b) SRC-Im-2: $|V_{em}|$ increasing from ± 1800 V to 2200 V in 100 V steps

Fig. 12 TOF traces when emitting EMI-Im. A tail of large mass-to-charge ratio species was particularly evident for negative polarity emissions.

negative polarities for all devices. The fractional deficit of EMI-Im devices was, on average, less than 3%, whereas for SRC-BF₄, larger reductions (in excess of 7%) were observed. These losses are relatively large compared with published results, indicating only a few volts of deficit [34,36]. In Table 4, the average fractionals $n = 0$ and $n = 1$ ΔV are listed for each polarity, facilitating inclusion in Eqs. (13) through (15).

The nonzero slopes between discrete ion masses can be attributed to fragmentation while accelerating between the emitter to extractor grid, where solvated ($n \geq 1$) ions break up into an ion and neutral components before complete acceleration [34,48]. In full-beam TOF, where a large detector collects the entire beam, similar drops just after each nominal flight time may manifest due to the spread in axial velocity [48]; however, here, we only sample a small portion of the beam passing within the 1.4 deg half-angle acceptance cone of the limiting aperture. Molecular dynamics simulations of fragmentation events [49] have indicated that breakup can be induced by both the ion's thermal energy and an applied electric field, and that the degree to which each process is dominant can differ between ion solvation numbers. Slopes in the TOF traces between the $n = 1$ to $n = 2$ expected masses, particularly for cations in Fig. 12, are relatively

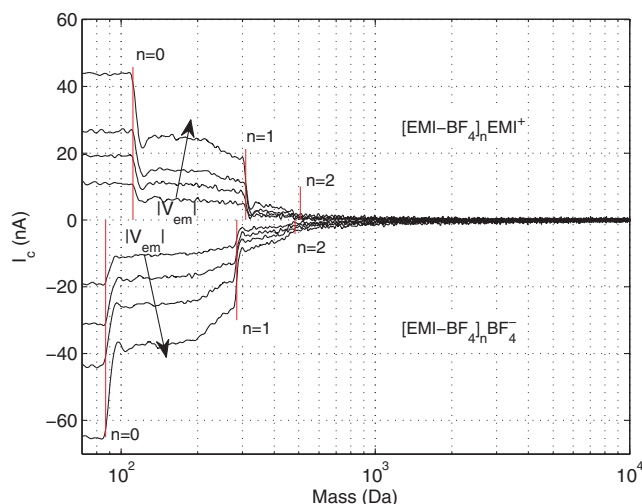


Fig. 13 TOF data from SRC-BF₄ with $|V_{em}|$ increasing from ± 2100 to 2400 V in 100 V steps. A relatively small population of high mass species was observed.

Table 3 Beam composition and energy deficits^a

Device	Ion	n	f_n , %	ΔV_{TOF} , V	$\frac{\Delta V_{TOF}}{V_{em}}$, %
SRC-Im-1	[EMI - Im] _n EMI ⁺	0	40 ± 3	55 ± 20	2.7 ± 0.8
		1	47 ± 3	30 ± 15	1.6 ± 0.7
		2	9.5 ± 2	—	—
		≥3	4 ± 1.5	—	—
SRC-Im-1	[EMI - Im] _n Im ⁻	0	40 ± 3	26 ± 4	1.2 ± 0.1
		1	40 ± 2	13 ± 3	0.6 ± 0.1
		2	10 ± 2	—	—
		≥3	10 ± 2	—	—
SRC-Im-2	[EMI - Im] _n EMI ⁺	0	44 ± 3	70 ± 45	2.3 ± 0.6
		1	44 ± 3	55 ± 40	1.3 ± 0.5
		2	9.5 ± 3	—	—
		≥3	3.5 ± 2	—	—
SRC-Im-2	[EMI - Im] _n Im ⁻	0	40 ± 4	23 ± 4	1.2 ± 0.2
		1	40 ± 4	14 ± 4	0.7 ± 0.1
		2	9 ± 3	—	—
		≥3	10 ± 3	—	—
SRC-BF ₄	[EMI - BF ₄] _n EMI ⁺	0	42 ± 2	160 ± 25	7.2 ± 1.1
		1	47 ± 3	140 ± 15	6.2 ± 0.7
		2	8.5 ± 2	—	—
		≥3	3.5 ± 2	—	—
SRC-BF ₄	[EMI - BF ₄] _n BF ₄ ⁻	0	44 ± 2	97 ± 9	4.2 ± 0.4
		1	44 ± 3	61 ± 6	2.7 ± 0.3
		2	8.5 ± 2	—	—
		≥3	4.5 ± 1.5	—	—

^aUncertainties indicate the standard deviation over 19 or more measurements.

consistent despite increasing emitter voltages. If ion breakup was dictated solely by a fixed time constant, a reduction in the degree of fragmentation during acceleration would be expected at higher voltages, as ions are more quickly swept out of the acceleration region. However, a corresponding increase in fragmentation due to higher external fields may counter this effect. Meanwhile, the relatively shallow slopes immediately after discrete steps in the trace (particularly $n = 0$) indicate ions have moved beyond the immediate vicinity of the emission site, where fields are strongest, before breaking up.

Although these observations thus imply further investigation is needed to describe ion fragmentation more completely, the RPA measurements presented in Sec. V.B.3 confirm kinetic energy deficits over a range consistent with this phenomenon. We have therefore applied fragmentation correction factors [Eqs. (4) and (5)], attributing nonzero slopes to fragmentation events alone: $n = 2 \rightarrow 1$ for $t_1 < t < t_2$ and $n = 1 \rightarrow 0$ for $t_0 < t < t_1$. The aggregate influence of these corrections (increases) on the metrics κ and ϕ have tended to be small, up to ~ 3 and 5% for the thrust and mass flow rate, respectively. However, the presented values have nonetheless been adjusted to include compensation for fragmentation for completeness.

Average propulsive parameters κ and ϕ , and the resultant polydispersive efficiency (κ^2/ϕ), are given in Table 4. Of particular relevance to our goal of comparing direct and indirect thrusts, the standard deviation of the parameter κ was, at most, $\sim 7\%$, despite the inelegance of averaging values over all voltage and beam angle measure-

Table 4 Summary of indirect propulsive parameters^a

Device	Polarity	κ	ϕ	$\frac{\kappa^2}{\phi}, \%$	$\langle \frac{\Delta V_{\text{TOF}}}{V_{\text{em}}} \rangle, \%$	$\langle \frac{\Delta V_{\text{RPA}}}{V_{\text{em}}} \rangle, \%$	θ_0, deg	$\theta_{\text{eff}}, \text{deg}$
SRC-Im-1	+	1.90 ± 0.06	5.1 ± 0.7	70 ± 11	2.1 ± 1.0	2.2 ± 0.9	$\parallel 0.1$ $\perp 2.0$	$\parallel 21.3$ $\perp 20.0$
	—	2.60 ± 0.18	9.8 ± 2.4	69 ± 19	0.9 ± 0.2	—	$\parallel 0.2$ $\perp 2.8$	$\parallel 22.4$ $\perp 21.2$
	—	—	—	—	—	—	—	—
SRC-Im-2	+	1.83 ± 0.06	4.8 ± 0.7	70 ± 12	1.8 ± 0.8	3.0 ± 0.8	$\parallel 4.5$ $\perp 10.5$	$\parallel 21.3$ $\perp 21.7$
	—	2.71 ± 0.19	11.7 ± 2.7	63 ± 17	0.9 ± 0.2	—	$\parallel 5.7$ $\perp 11.7$	$\parallel 21.6$ $\perp 22.0$
	—	—	—	—	—	—	—	—
SRC-BF ₄	+	1.48 ± 0.02	2.6 ± 0.3	83 ± 9	6.7 ± 1.3	—	$\parallel 5.5$	$\parallel 20.8$
	—	1.45 ± 0.03	2.7 ± 0.3	77 ± 9	3.5 ± 0.4	—	$\parallel 3.4$	$\parallel 20.2$

^aUncertainties indicate the standard deviation over 19 or more measurements

ment conditions. Relatively large fluctuations in ϕ contributed to the large propagated errors in polydisperse efficiency reported. Regardless, the comparatively large polydisperse efficiencies measured when emitting EMI-BF₄ are consistent with emissions within or close to the PIR [7,16,41]. Conversely, the larger spread in constituent masses and possible droplet tail, after removing offsets, observed from both EMI-Im sources contributed to lower efficiency. For those devices, the negative polarity mass flow rate, proportional to the factor ϕ , was roughly double that at positive potential. Within the standard deviations quoted, all parameters measured from both devices emitting EMI-Im were consistent.

2. Angular Current Distribution

Figure 14 provides examples of the collected current to emitted current fraction versus thruster angle with the axis of rotation orientated parallel and perpendicular to the emission strips. Parallel rotations were recorded from all devices, whereas perpendicular rotations were only measured from SRC-Im-1 and SRC-Im-2. The prevalence of multiple Taylor cones (emission sites) per emitter structure in porous ILISs in [24] has driven the development of the linear emission strip geometry. However, that same work found that emission sites were expected wherever the field was strong enough and might, as a result, not be well aligned axially. In this context, the reasonably well-collimated beams shown are a welcome confirmation that conventional machining can produce sufficiently sharp structures to avoid wide beam angles.

For all devices, more current relative to that emitted was collected in the negative polarity versus positive. As shown by the indicated insets in Figs. 14a and 14b, the two polarities are nevertheless in agreement when scaled by their respective maxima. Considering the five 81% geometric transparency grids between the source and detector and the finite source dimensions, the negative current was typically consistent with sampling the entire beam with a source misalignment of a few millimeters. The reduction in positive current

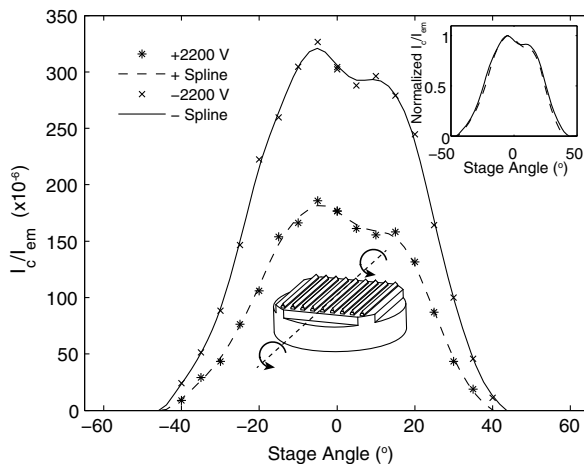
may be attributed to neutralization by secondary electrons born from the impact of ions on the baffles and aperture plate surrounding the narrow TOF tube inlet aperture.

An axisymmetric approximation was made from each set of bidirectional rotation data, facilitating use of the right-hand side of Eq. (12). This process included determining an offset angle θ_0 , taken as that angle about which axisymmetric surface integrations using relatively positive or negative rotation angles are equal. These two halves were then averaged to yield a single representative profile for each orientation and/or voltage.

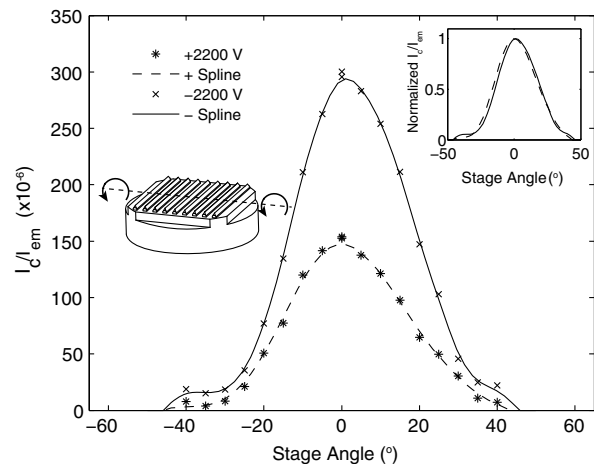
Given the inconsistency between the integrated and expected beam currents, axisymmetric approximations for each device/polarity have been normalized such that the integration of $\bar{j}(\theta)$ over S is unity. The effective beam angle has then been calculated by Eq. (12); see Table 4. In the table, \parallel and \perp indicated rotations parallel and perpendicular to the emitter strips, respectively. Measurements repeated at differing emitter voltages were consistent to within ~ 2 deg. The effective cone angle θ_{eff} was close to 21 deg for all cases, corresponding to a loss of $\sim 7\%$ in thrust output compared with a perfectly collimated beam. The consistency in θ_{eff} between rotation orientations, despite a more narrow profile in Fig. 14b versus Fig. 14a, reflects the diminishing returns, in terms of propulsive performance, achieved when collimating the central portion of the beam. Rather, the small current contributions beyond ~ 35 deg, in both orientations, are a relatively significant inefficiency driver.

3. Energy Spectra

RPA data were limited to constant positive V_{em} and zero rotation angle. The data (see Fig. 15) confirm a primary population of particles had energies close to that of the emitters. However, a significant portion of the collected beam was, apparently, repelled at a lower energy. In [34,36], low-energy beam repulsion was attributed to downstream ion fragmentation. However, downstream fragmentation manifests as a relatively discrete step/peak at a known energy



a) Rotation parallel to the strip edges



b) Rotation perpendicular to the strip edges

Fig. 14 Beam current fractions versus angle when rotating on the indicated axes. The inset figures demonstrate that normalized data are consistent.

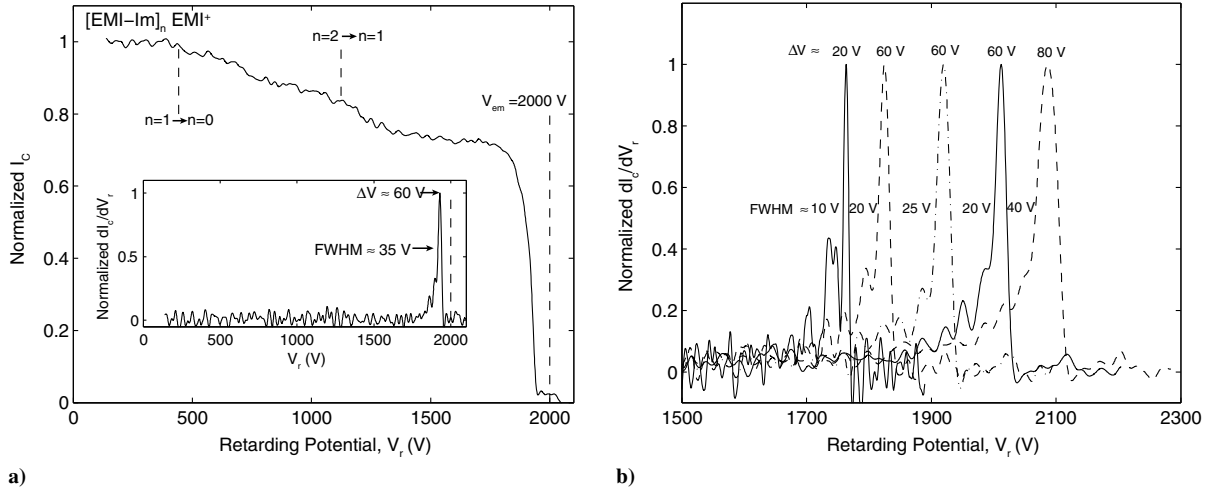


Fig. 15 Representations of a) smoothed current data measured against the retarding potential from SRC-Im-1, where vertical lines indicate the anticipated location of peaks associated with downstream (of the extractor) solvated ion breakup; and b) distributions of current over retarding potential from SRC-Im-2.

corresponding to breakup in a field-free region. The expected peak locations due to such events are readily determined by scaling the initial particle energy qV_{em} by the ratio of post- to pre-breakup ion mass [34]. Specifically, if a solvated ion of mass m_n has kinetic energy qV_{em} and breaks into a charged particle of mass m_{n-1} and a neutral of mass $m_n - m_{n-1}$, the charged particle (ion) will have energy K_{n-1} given by Eq. (16):

$$K_{n-1} = \frac{m_{n-1}}{m_n} qV_{em} \quad (16)$$

Emitting positive EMI-Im ions, the postfragmentation ion energies will then be only 22 and 56% of the initial kinetic energy after $n = 1 \rightarrow 0$ and $n = 2 \rightarrow 1$ transitions, respectively. These energy levels are indicated in Fig. 15a. Although the $n = 1 \rightarrow 0$ marker did tend to indicate the lower limit of species energy, prominent peaks were not observed. In addition to breakup within the emitter to extractor accelerator region, as discussed in the context of the aforementioned TOF measurements, these measurements could therefore indicate that significant fragmentation occurred within the RPA's deceleration field. Compared with [34], the RPA setup here did not include an upstream einzel lens, and was therefore positioned closer to the source. Ultimately, the physical extent of the multiple retarding grids was roughly equal to the flight distance before the RPA. Hence, relatively little flight distance/time was available for

breakup to occur downstream of the extractor grid yet before entering the probe.

The peak energy deficit was found to be typically within 20 to 80 V of V_{em} after correction for the current monitor resistance. These small deficits (a few percent of the emitter voltage) are in reasonable agreement with the average deficits estimated by TOF; see Table 4. However, they are, again, large compared with previous studies of ILISs emitting EMI-Im. Specifically, Lozano [34] measured only a few (~ 5 – 7 V) volt deficits and full width at half-maximum (FWHM) of similar order. Here, the FWHM was typically ~ 10 – 40 V. The same instructions [47] were applied to our RPA and that of Lozano [34]. Hence, we anticipated a similar high-resolution probe; however, it should be noted that the resolution of our RPA was not rigorously verified with a monoenergetic reference source.

VI. Discussion

A. Comparison of Direct and Indirect Thrust Measurements

Direct (DTM) and indirect (ITM) thrust measurements are plotted for each of the three tested devices in Figs. 16 and 17. The ITMs correspond to $T_{ITM} = \alpha T^+ + (1 - \alpha) T^-$, where the thrusts T^\pm for each polarity were determined through Eq. (13) using the indirect propulsive parameters listed in Table 4 and the factor $I_b \sqrt{|V_{em}|}$ measured at each direct thrust measurement. Averaged input powers are indicated in the figure insets. All devices generated tens of micronewtons with less than 0.8 W of input power. Maximum thrust

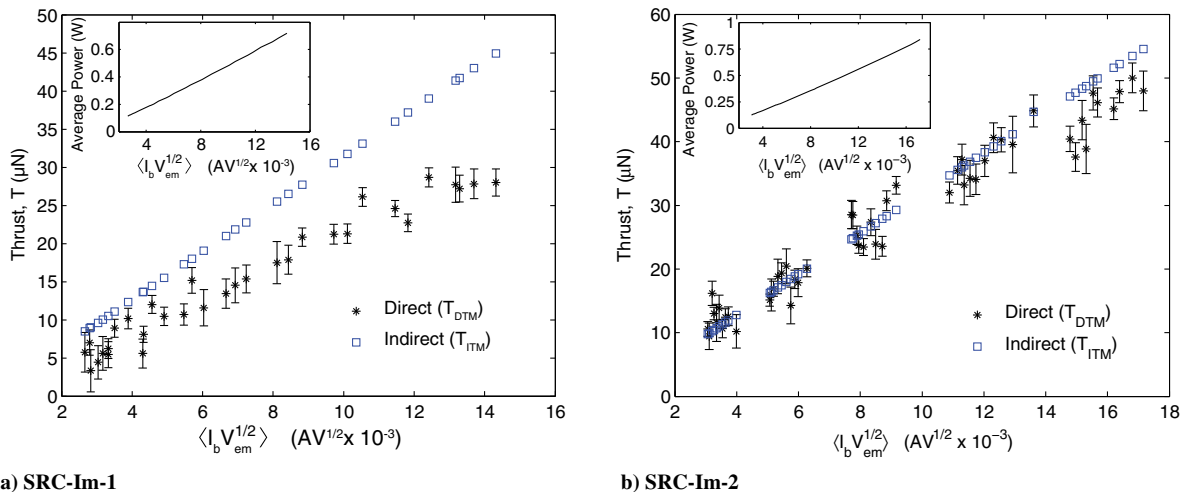


Fig. 16 Directly (DTM) and indirectly (ITM) measured thrusts from devices wet with EMI-Im. The indirect thrust measurement standard error was $\sim \pm 2$ – 3 μ N.

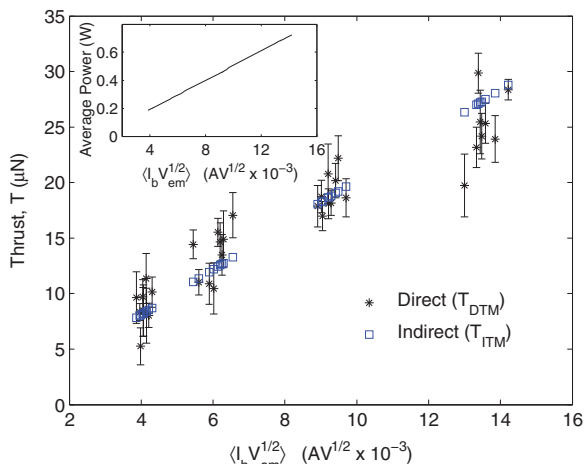


Fig. 17 Directly (DTM) and indirectly (ITM) measured thrusts from SRC-BF₄. The indirect thrust measurement standard error was $\sim \pm 1 \mu\text{N}$.

levels of $\sim 50 \mu\text{N}$ and $\sim 30 \mu\text{N}$ were measured when emitting the ILs EMI-Im and EMI-BF₄, respectively. Higher thrusts from EMI-Im were anticipated due to the higher anion mass.

The directly measured and indirectly calculated thrusts from SRC-Im-2 and SRC-BF₄ were in good agreement for all but the highest emission levels. Specifically, the values agreed to within a few micronewtons up to $\sim 40 \mu\text{N}$ and $\sim 20 \mu\text{N}$ for SRC-Im-2 and SRC-BF₄, respectively, with deviations closer to $5 \mu\text{N}$ at higher thrust levels. Less consistent agreement was observed from SRC-Im-1 where disparities approached $15 \mu\text{N}$ at high power.

The predicted thrusts tended to exceed that emitted at high current. The composition, angle, and energy thrust coefficients have been approximated as constant averages over all voltages and angles. We therefore only consider the bulk standard deviations in κ listed in Table 4, which correspond to up to $\sim 3 \mu\text{N}$, as providing bounds to the calculations. If more consistent TOF measurements had been obtained, the divergence at high voltage may have been reduced through parameterizing κ versus voltage. Regardless, lower than expected thrusts were supportive of highly ionic emissions since an undetected droplet population would have lead to a higher thrust.

Inadequate thrust balancing may have contributed to the disagreement in Fig. 16a for SRC-Im-1. Referring to Table 4, the ratio of positive to negative κ parameters calculated by TOF was approximately ~ 0.7 for both SRC-Im-1 and SRC-Im-2, and it was ~ 1.0 for device SRC-BF₄. The ratios applied to establish DTM setpoints (Table 2) were similar for SRC-Im-2 and SRC-BF₄, yet SRC-Im-1 may have been relatively poorly balanced. In all cases, force imbalances have been accounted for in T_{ITM} to a degree through the duty-cycle weighted average described; however, the response of the balance to pulsations, as may have been particularly present with SRC-Im-1, was unknown.

B. Compiled Thruster Performance

The agreements between direct and indirect thrust measurements from the same devices (a unique scenario for a passively fed and ionic electrospray thruster) permit total performance estimates. In Table 5, we have interpolated the propulsive efficiency, specific impulse, and thrust at 0.5 W of input power. The specific impulse and propulsive efficiency have been calculated by Eqs. (14) and (15), modified to

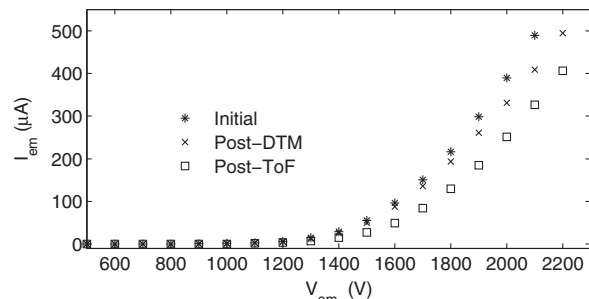


Fig. 18 Emission currents at a given emitter voltage tended to decay over the course of measurements.

account for potential alternation. For all devices, values in parentheses were obtained when using an interpolation of the directly measured thrust, although the calculated mass flow was used for all values. In this form, the data reaffirm the improved specific performance of EMI-BF₄ over EMI-Im, at the expense of reduced thrust, due to greater ion content and lower anion mass associated with EMI-BF₄ emissions. Given the comprehensive nature of the diagnostic measurements presented, and good agreement with direct measurements for two of the three devices, we are confident that these performance metrics present an accurate portrayal of the capabilities available from such a device.

In interpreting these data, the implicit scalability of ILIS thrusters should be considered. The active area of these prototype devices was roughly 1 cm^2 ; hence, numerous sources could be accommodated within a small area, thereby increasing the thrust. Indeed, to obtain charge neutrality, the intended application would include at least two sources operated simultaneously at opposite polarities.

Referring to Eq. (15) and Table 4, it is clear that polydisperse efficiency represents the greatest inefficiency within the system, which is consistent with the efforts to increase this parameter, discussed in the Introduction (Sec. I). Beam spreading and interception by the extraction grid were the next most significant contributors, respectively, although for SRC-BF₄, energy deficit losses also approached 7%. Grid interception must be reduced through design improvements, not only to improve performance but to eliminate erosion as a lifetime limitation. Meanwhile, beam spread over angle would be improved to a degree if a downstream secondary accelerating electrode were included [26], although the efficiency benefits would likely be small. The higher-energy deficits compared with the literature should be further explored. The ill-defined IL to aluminum contact made through the guard ring may have contributed to this loss, although the deficits were only weakly correlated with V_{em} (and therefore I_{em}), indicating loss mechanisms were not entirely ohmic. Despite these losses, when compared with other miniaturized ion propulsion systems [11], and considering the system benefits of completely passive (unpowered) propellant feeding, the high specific impulses and ~ 50 to 65% power efficiencies achieved with these prototypes are encouraging.

C. Emission Decay and Longevity

This initial study has been intended to confirm the efficacy of indirect thrust measurements and to demonstrate that a simple fabrication process can be used to form high-current porous emission sources. Many design improvements are required to transition from these demonstration thrusters to engineering breadboards suitable for long-duration tests and precise thrust resolution measurements. Decays in emission current over the course of the test campaign were a particular concern. Figure 18 provides an example of the decrease in emitted current before and after direct thrust measurements at ESTEC, and subsequently after TOF measurements at EPFL. It is tempting to broadly attribute this behavior to degradation due to electrochemical reactions at the ionic liquid to guard ring contact interface [2,44]. We have followed the most recent recommendations in the literature whenever possible: use of a glass emitter substrate enforced a distal electrical contact [46], and attempts were made to balance positive and negative emission charge transfers over each

Table 5 Thruster performance summary at 0.5 W^a

Device	$T, \mu\text{N}$	I_{sp}, s	$\eta_{\text{prop}}, \%$
SRC-Im-1	33 (23)	1660 (1120)	53 (25)
SRC-Im-2	35 (34)	1440 (1410)	49 (47)
SRC-BF ₄	20 (20)	3260 (3290)	65 (66)

^aParentheses indicate values calculated by interpolation of DTM.

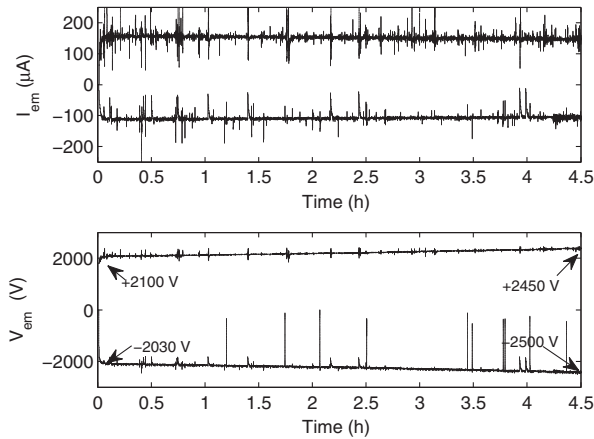


Fig. 19 Emission over 4.5 h while maintaining a calculated $15 \mu\text{N}$ of thrust through closed-loop feedback control of $(I_b \sqrt{|V_{em}|})$.

period of potential alternation during thrust measurements [33,50]. However, long (greater than 10 s) periods of sustained unipolar operation were unavoidable with the TOF and RPA systems as configured, and the efficacy of potential alternation to suppress reactions was not confirmed within our specific application. If, for example, reactions were occurring at the ill-defined aluminum to IL interface, the effective current path resistance could have been increasing, despite the absence of breakdowns at the glass emission sites. To gain further insight into emission decays, we operated SRC-Im-1 continuously for greater than 4.5 h at 1 Hz and with a closed-loop feedback mechanism to ensure constant charge balance while also attempting to maintain $20 \mu\text{N}$ of predicted thrust output in each polarity through constant $\pm I_b \sqrt{|V_{em}|}$ setpoints. The current and voltage in each polarity are presented in Fig. 19 over the course of the test. The voltage required to sustain the commanded thrust rose steadily from +2100/−2030 to +2450/−2500 V, whereas the current decayed accordingly. It is notable that the average power rose less dramatically, from ~ 0.29 to ~ 0.32 W. The current spikes visible were, in part, indications of deficiencies in the simple controller employed, which could not rapidly suppress surges.

The test was ended intentionally, no specific or dramatic failure mode was encountered, and liquid remained in the device. The total time required to deplete the available propellant was calculated using Eq. (7), with the coefficients ϕ listed in Table 4 and the average currents measured during this test. If the device was freshly loaded with the initial 110 to 120 μL of EMI-Im, all liquid would have been consumed after approximately 40 h. In actuality, the device had already been operated for approximately 2 h during the thrust and diagnostic data acquisitions before beginning this test. However, even considering this time, many more hours would have been required to exhaust all available propellant.

At the culmination of the test, we inspected the device. Most evidently, the extractor grids were eroded near the emitter strip ends

and the previously white/clear surface was distinctly yellow. Erosion was not unexpected at these positions since the emitting strips terminate abruptly at each end, resulting in sharp features perpendicular to the desired orientation. Emissions from these ends had struck the extractor grid and, after several hours, caused significant erosion. The accompanying sputtered material may also be responsible for some of the observed discoloration and, possibly, current decay through contamination of the emitting surfaces.

D. Triangular Prisms as Emission Sources

The conventional machining approach applied was successful in obtaining up to 500 μA of highly ionic emission from 1-cm-diam active areas, with current densities similar to reported measurements from hundreds of axisymmetric porous emitters multiplexed in arrays [2,5]. The number of active emission sites was not confirmed directly. Maximum reported currents from individual axisymmetric porous emitters have ranged from hundreds of nanoamperes [5] to more than 5 μA [23]. The hundreds of microamperes reported here are therefore broadly indicative of activating several hundred emission sites over the nine emitting edges. However, the number of sites per structure in the literature has not been reported with certainty. Furthermore, a definitive or phenomenological maximum current level was not reached here, nor has one been typically reported from previously reported devices using structures with a porous bulk material. Correspondingly, detailed quantitative comparisons between current levels and emitter densities in the literature as a means to calculate emission site distributions are imprudent at present.

As local field strengths will have exceeded the minimum threshold for emission at differing voltages along the undulated edges, the number of active sites likely increased with voltage. Further study is required to establish criteria for emission site spacing, accounting for potential hydrodynamic interactions, and space charge effects along with the local electrostatics. Such an understanding will be important in developing the design. For example, the emitting edges protruded into the grid thickness for both EMI-Im devices. Some emissions from sites off the symmetry axis of those devices may have been lost due to strong electric fields oriented toward the grid walls. As with misguided emissions from the ends of each strip, resultant sputtered material or secondary electrons could have interacted with the nearby IL and may have contributed to the degrading emission over time. Enhanced knowledge of emission site localization may also be beneficial to interpreting fragmentation events through providing an improved understanding of the electric field each particle experiences after emission.

TOF measurements were made at differing emitter voltages and beam angles. However, all measurements were averaged to provide single propulsive metrics for each device and polarity. This decision was made for two reasons. First, the beam current decays over the course of TOF measurements resulted in ambiguity when attempting to attribute voltage resolved TOF parameters with the conditions present during DTM. Second, any changes in propulsive metrics that were observed tended to be relatively small and comparable to the

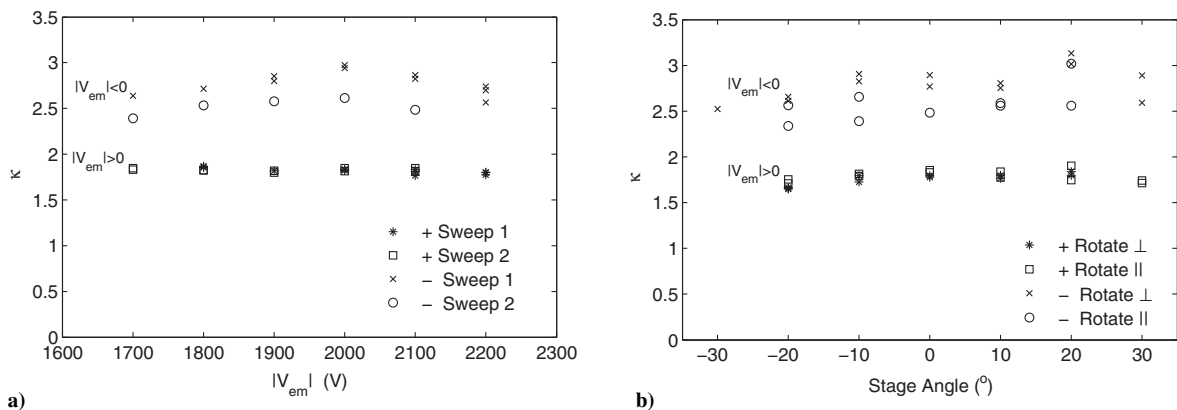


Fig. 20 Small and inconsistent trends observed when measuring the TOF parameter κ at a) differing voltages and b) beam angles. In Fig. 20a, sweeps indicate repeated data acquisition under the same conditions.

deviations inherent when repeating measurements at consistent inputs. Specifically, no clear trends were visible in beam composition versus extraction voltage nor angle, via either the thrust metric κ nor the mass flow rate factor ϕ . For example, Figs. 20a and 20b demonstrate the calculated parameter κ versus voltage (at 0 deg) and versus angle, respectively, from SRC-Im-2.

The lack of trend versus beam angle result would be particularly noteworthy for an individual emitter or an array of geometrically identical emitters. Previous studies have, for example, found significant trends in mass flow rate (droplet content) versus angle from individual ILISs [37]. However, measurements versus angle here comprise a summation of currents due to beamlets originating at different surface angles and with differing intensities due to the lack of enforced emission site localization on the porous surface.

VII. Conclusions

A simple-to-fabricate ionic electrospray thruster with fully passive propellant feeding has been presented. A small yet conventional computer numerical control mill was used to machine triangular prisms, $\sim 300\ \mu\text{m}$ tall and with an apex radius of curvature of roughly $10\text{--}30\ \mu\text{m}$, from commercially available porous borosilicate filter disks. Three prototype thrusters have been tested: two emitting the ionic liquid EMI-Im, and one using EMI-BF₄. For all sources, several hundred microamperes were emitted from less than $1\ \text{cm}^2$ of active area at voltages near 2000 V. Despite limited control over the emitting apex curvature, the emission spread over angle was equivalent to an $\sim 21^\circ$ deg hollow cone, representing a small $\sim 7\%$ reduction in thrust over a perfectly collimated beam.

The utility of such a source as a compact thruster has been demonstrated through direct thrust measurements. Controllable thrusts from 5 to 50 μN , corresponding to 0.1 to 0.8 W, were recorded when emitting EMI-Im and from 7 to 25 μN at 0.2 to 0.7 W when emitting EMI-BF₄. These data were measured while alternating the emission polarity at 1 Hz while attempting to balance total charge emission through appropriate selection of the duty cycle, in an effort to suppress electrochemical degradation. The thrusters were controlled by an applied emitter to extractor grid voltage alone; propellant IL was passively drawn from an integral porous reservoir.

Accurate calculation of thrust using indirect probe measurements has been discussed and demonstrated. Through defining nondimensional modifiers describing the average mass-to-charge ratio of constituent beam particles, an effective beam angle, and energy deficits compared with the applied voltage, calculations of thrust output have been made as a function of beam current and emission voltage. For two of three devices, these calculations matched the directly measured thrust to within a few micronewtons. Specifically, it has been shown that, although time-of-flight spectrometry alone can provide a thrust estimate close to that directly measured, modifications due to beam angle and energy deficits should be included to obtain good accuracy. The effects of fragmentation within the emitter to extractor grid were also considered, yet were found to have a small ($\sim 3\%$) influence on thrust.

The mass flow rate has been similarly calculated using time-of-flight measurements, and the results have been applied, along with thrust, to calculate the expected specific impulse and total propulsive efficiencies of the prototype thrusters. Emissions from EMI-Im included a small droplet, or highly solvated ion, content, representing up to 10% of the total current during negative polarity operation. This population contributed to relatively low calculated propulsive efficiencies and specific impulses: roughly 50% and 1500 s at 0.5 W from devices emitting EMI-Im. Conversely, spectra from EMI-BF₄ emissions revealed a lower intensity (less than 4.5%) and lower mass solvated ion tail, which was consistent with this liquid approaching the purely ionic regime. Consequently, higher propulsive efficiency (65%) and specific impulse (3260 s) were calculated.

These novel, conventionally machined thrusters can enable low-cost and accessible study of the operation of porous IL electrospray sources without an emphasis on device fabrication, beginning with this study of thrust and propulsive performance. It is intended to continue these investigations through 1) developing the device de-

sign, in order to increase the operational lifetime and improve emission consistency; and 2) continued efforts to seek experimental evidence of the predicted performance benefits of ILIS thrusters. The latter will include measurements of thrust output while simultaneously emitting balanced currents, of opposite polarity, in order to confirm charge neutralization and measurements of true specific impulse by directly recording the propellant mass reduction over very long durations while monitoring thrust.

Acknowledgments

This work has been supported through ESA Networking/Partnership Initiative contract number 4000109063/13/NL/PA. The authors would like to thank Alexandra Bulit, Davina Di Cara, Kathe Dannenmayer, and Eduard Bosch Borrás of the ESA Propulsion Laboratory for their assistance with the direct thrust measurements.

References

- [1] Gassend, B., Velasquez-Garcia, L. G. M., and Martinez-Sanchez, A. I. A., "A Microfabricated Planar Electrospray Array Ionic Liquid Ion Source with Integrated Extractor," *Journal of Microelectromechanical Systems*, Vol. 31, No. 6, 2009, pp. 679–694. doi:10.1109/JMEMS.2009.2015475
- [2] Courtney, D. G., Li, H. Q., and Lozano, P., "Emission Measurements from Planar Arrays of Porous Ionic Liquid Ion Sources," *Journal of Physics D: Applied Physics*, Vol. 45, No. 48, 2012, Paper 485203. doi:10.1088/0022-3727/45/48/485203
- [3] Stark, J., Stevens, B., Alexander, M., and Kent, B., "Fabrication and Operation of Microfabricated Emitters as Components for a Colloid Thruster," *Journal of Spacecraft and Rockets*, Vol. 42, No. 4, 2005, pp. 628–639. doi:10.2514/1.7537
- [4] Kpoun, R., and Shea, H. R., "Integrated Out-of-Plane Nano-electrospray Thruster Arrays for Spacecraft Propulsion," *Journal of Micromechanics and Microengineering*, Vol. 19, No. 4, 2009, Paper 045019. doi:10.1088/0960-1317/19/4/045019
- [5] Coffman, C., Perna, L., Li, H., and Lozano, P. C., "On the Manufacturing and Emission Characteristics of a Novel Borosilicate Electrospray Source," *49th AIAA Joint Propulsion Conference and Exhibit*, AIAA Paper 2013-4035, 2013.
- [6] Romero-Sanz, I., Bocanegra, R., Gamero-Castaño, M., de la Mora, J. F., and Lozano, P., "Source of Heavy Molecular Ions Based on Taylor Cones of Ionic Liquids Operating in the Pure Ion Evaporation Regime," *Journal of Applied Physics*, Vol. 94, No. 5, 2003, pp. 3599–3605. doi:10.1063/1.1598281
- [7] Lozano, P., and Martinez-Sánchez, M., "Ionic Liquid Ion Sources: Characterization of Externally Wetted Emitters," *Journal of Colloid and Interface Sciences*, Vol. 282, No. 2, 2005, p. 415–421. doi:10.1016/j.jcis.2004.08.132
- [8] Lozano, P., and Martinez-Sánchez, M., "Efficiency Estimation of EMI-BF₄ Ionic Liquid Electrospray Thrusters," *41st Joint Propulsion Conference and Exhibit*, AIAA Paper 2005-4388, 2005.
- [9] Taylor, G. I., "Disintegration of Water Drops in an Electric Field," *Proceedings of the Royal Society of London Series A: Mathematical and Physical Sciences*, Vol. 280, No. 1382, 1964, pp. 383–397.
- [10] Warner, N. Z., "Theoretical and Experimental Investigation of Hall Thruster Miniaturization," Ph.D. Thesis, Massachusetts Inst. of Technology, Cambridge, MA, 2007.
- [11] Mueller, J., Hofer, R., and Ziemer, J., "Survey of Propulsion Technologies Applicable to Cubesats," NASA TR 10-1646, 2010.
- [12] Dandavino, S., "Microfabricated Electrospray Thrusters for a Modular Spacecraft Propulsion System," Ph.D. Thesis, École Polytechnique Fédérale de Lausanne, Neuchâtel, Switzerland, 2014.
- [13] Ziemer, J. K., and Merkwitz, S. M., "Microthruster Propulsion for the LISA Mission," *40th Joint Propulsion Conference*, AIAA Paper 2004-3439, 2004.
- [14] Marcuccio, S., Giusti, N., and Pergola, P., "Slit FEED Thruster Performance with Ionic Liquid Propellant," *49th AIAA Joint Propulsion Conference and Exhibit*, AIAA Paper 2013-4034, 2013.
- [15] Tajmar, M., Vasiljevich, I., Plesescu, F., Griener, W., Buldrini, N., Betto, M., and del Amo, J. G., "Development of a Porous Tungsten mN-FEEP Thruster," *Proceedings of the Space Propulsion Conference*, San Sebastian, Spain, 2010.
- [16] Legge, R. S., and Lozano, P. C., "Electrospray Propulsion Based on Emitters Microfabricated in Porous Metals," *Journal of Propulsion and*

- Power*, Vol. 27, No. 2, 2011, pp. 485–495.
doi:10.2514/1.50037
- [17] Hill, F. A., Leon, P. P. D., and Velásquez-García, L. F., “High-Throughput Ionic Liquid Electrospray Sources Based on Dense Monolithic Arrays of Emitters with Integrated Extractor Grid and Carbon Nanotube Flow Control Structures,” *17th International Conference on Solid-State Sensors, Actuators and Microsystems, Transducers 2013*, IEEE Publ., Piscataway, NJ, 2013, pp. 2644–2647.
 - [18] Ziemer, J. K., Randolph, T. M., Franklin, G. W., Hruby, V., Spence, D., Demmons, N., Roy, T., Ehrbar, E., Zwahlen, J., Martin, R., and Connolly, W., “Colloid Micro-Newton Thrusters for the Space Technology 7 Mission,” *IEEE Aerospace Conference 2010*, IEEE Publ., Piscataway, NJ, 2010; also AERO Paper 2010-5446760, 2010.
 - [19] Gamero-Castaño, M., and Hruby, V., “Electrospray as a Source of Nanoparticles for Efficient Colloid Thrusters,” *Journal of Propulsion and Power*, Vol. 17, No. 5, 2001, pp. 977–987.
doi:10.2514/2.5858
 - [20] Alonso-Matilla, R., Fernández-García, J., Congdon, H., and de la Mora, J. F., “Search for Liquids Electrospraying the Smallest Possible Nanodrops in Vacuo,” *Journal of Applied Physics*, Vol. 116, No. 22, 2014, Paper 224504.
doi:10.1063/1.4901635
 - [21] Lenguito, G., and Gomez, A., “Development of a Multiplexed Electrospray Micro-Thruster with Post-Acceleration and Beam Containment,” *Journal of Applied Physics*, Vol. 114, No. 15, 2013, Paper 154901.
doi:10.1063/1.4822029
 - [22] Ryan, C., Daykin-Iliopoulos, A., Stark, J. P. W., Salaverri, A., Vargas, E., Rangsten, P., Dandavino, S., Ataman, C., Chakraborty, S., Courtney, D., and Shea, H., “Experimental Progress Towards the MicroThrust MEMS Electrospray Electric Propulsion System,” *Proceedings of the 33rd International Electric Propulsion Conference*, International Rocket Propulsion Soc., Fairview Park, OH, 2013; also IEPC Paper 2013-146, 2013.
 - [23] Courtney, D. G., and Lozano, P., “Characterization of Conical Ionic Liquid Ion Sources for 2-D Electrospray Thruster Arrays on Porous Substrates,” *Transactions of the Japan Society for Aeronautical and Space Sciences, Aerospace Technology Japan*, Vol. 8, No. ists27, 2010, pp. Pb_73–Pb_78.
doi:10.2322/tastj.8.Pb_73
 - [24] Courtney, D. G., “Ionic Liquid Ion Source Emitter Arrays Fabricated on Bulk Porous Substrates for Spacecraft Propulsion,” Ph.D. Thesis, Massachusetts Inst. of Technology, Cambridge, MA, 2011.
 - [25] Deng, W., Klemic, J. F., Li, X., Reed, M. A., and Gomez, A., “Increase of Electrospray Throughput Using Multiplexed Microfabricated Sources for the Scalable Generation of Monodisperse Droplets,” *Aerosol Science*, Vol. 37, No. 6, 2006, pp. 696–714.
doi:10.1016/j.jaerosci.2005.05.011
 - [26] Dandavino, S., Ataman, C., Ryan, C. N., Chakraborty, S., Courtney, D. G., Stark, J. P. W., and Shea, H., “Microfabricated Electrospray Emitter Arrays with Integrated Extractor and Accelerator Electrodes for the Propulsion of Small Spacecraft,” *Journal of Micromechanics and Microengineering*, Vol. 24, No. 7, 2014, Paper 075011.
 - [27] Courtney, D. G., Li, H. Q., and Lozano, P., “Electrochemical Micromachining on Porous Nickel for Arrays of Electrospray Ion Emitters,” *Journal of Microelectrochemical Systems*, Vol. 22, No. 2, 2013, pp. 471–482.
doi:10.1109/JMEMS.2012.2227951
 - [28] Meyer, I. V., Edmond, J., and King, L. B., “Electrospray from an Ionic Liquid Ferrofluid Utilizing the Rosensweig Instability,” *49th Joint Propulsion Conference and Exhibit*, AIAA Paper 2013-3823, 2013.
 - [29] Lozano, P., Martínez-Sánchez, M., and López-Urdiales, J. M., “Electrospray Emission from Nonwetting Flat Dielectric Surfaces,” *Journal of Colloid and Interface Sciences*, Vol. 276, No. 2, 2004, pp. 392–399.
doi:10.1016/j.jcis.2004.04.017
 - [30] Perel, J., Mahoney, J. F., Moore, R. D., and Yahiku, A. Y., “Research and Development of a Charged-Particle Bipolar Thruster,” *AIAA Journal*, Vol. 7, No. 6, 1969, pp. 507–511.
doi:10.2514/3.5137
 - [31] Legge, R., and Lozano, P., “Performance of Heavy Ionic Liquids with Porous Metal Electrospray Emitters,” *44th Joint Propulsion Conference and Exhibit*, AIAA Paper 2008-5002, 2008.
 - [32] Courtney, D. G., and Shea, H., “Fragmentation in Time-of-Flight Spectrometry-Based Calculations of Ionic Electrospray Thruster Performance,” *Journal of Propulsion and Power*, Vol. 31, No. 5, 2015, pp. 1500–1504.
 - [33] Castro, S., and de la Mora, J. F., “Effect of Tip Curvature on Ionic Emission from Taylor Cones of Ionic Liquids from Externally Wetted Tungsten Tips,” *Journal of Applied Physics*, Vol. 105, No. 6, 2009, Paper 034903.
doi:10.1063/1.3073873
 - [34] Lozano, P., “Energy Properties of an EMI-Im Ionic Liquid Ion Source,” *Journal of Physics D: Applied Physics*, Vol. 39, No. 1, 2006, pp. 126–134.
doi:10.1088/0022-3727/39/1/020
 - [35] Chakraborty, S., Ataman, C., Dandavino, S., and Shea, H., “Micro-fabrication of an Electrospray Thruster for Small Spacecraft,” *Proceedings of POWERMEMS*, Transducers Research Foundation, San Diego CA, 2012, pp. 2–5.
 - [36] Fedkiw, T. P., and Lozano, P. C., “Development and Characterization of an Iodine Field Emission Ion Source for Focused Ion Beam Applications,” *Journal of Vacuum Science and Technology, B*, Vol. 27, No. 6, 2009, pp. 2648–2653.
doi:10.1116/1.3253604
 - [37] Chiu, Y.-H., Gaeta, G., Levandier, D. J., Dressler, R. A., and Boatz, J. A., “Vacuum Electrospray Ionization Study of the Ionic Liquid, [Emim] [Im],” *International Journal of Mass Spectrometry*, Vol. 265, No. 2, 2007, pp. 146–158.
doi:10.1016/j.ijms.2007.02.010
 - [38] Martínez-Sánchez, M., “MIT Course 16.522, Space Propulsion Notes,” MIT Open Courseware [online database], <http://ocw.mit.edu> [retrieved Jan. 2015].
 - [39] Ziemer, J. K., “Performance of Electrospray Thrusters,” *Proceedings of the 31st International Electric Propulsion Conference*, International Rocket Propulsion Soc., Fairview Park, OH, 2009; also IEPC Paper 2009-242, 2009.
 - [40] Lozano, P., and Martínez-Sánchez, M., “Studies on the Ion-Droplet Mixed Regime in Colloid Thrusters,” Ph.D. Thesis, Massachusetts Inst. of Technology, Cambridge, MA, 2003, <http://ssl.mit.edu/files/website/theses/PhD-2003-Lozano-TovarPaulo.pdf>.
 - [41] Kpoun, R., Smith, K. L., Stark, J. P. W., and Shea, H., “Tailoring the Hydraulic Impedance of Out-of-Plane Micromachined Electrospray Sources with Integrated Electrodes,” *Applied Physics Letters*, Vol. 94, No. 16, 2009, Paper 163502.
doi:10.1063/1.3117191
 - [42] Khayms, V., “Advanced Propulsion for Microsatellites,” Ph.D. Thesis, Massachusetts Inst. of Technology, Cambridge, MA, 2000.
 - [43] Larriba, C., Garoz, D., Bueno, C., Romero-Sanz, I., Castro, S., and de la Mora, J. F., “Taylor Cones of Ionic Liquids as Ion Sources: The Role of Electrical Conductivity and Surface Tension,” *Ionic Liquids: Not Just Solvents Anymore*, edited by Brennecke, J. F., Rogers, R. D., and Seddon, K. R., Oxford Univ. Press, New York, 2007, pp. 308–319, Chap. 21.
doi:10.1021/bk-2007-0975.ch021
 - [44] Lozano, P., and Martínez-Sánchez, M., “Ionic Liquid Ion Sources: Suppression of Electrochemical Reactions Using Voltage Alternation,” *Journal of Colloid and Interface Sciences*, Vol. 280, No. 1, 2004, pp. 149–154.
doi:10.1016/j.jcis.2004.07.037
 - [45] de la Mora, J. F., Berkel, G. J. V., Enke, C., Cole, R. B., Martínez-Sánchez, M., and Fenn, J. B., “Electrochemical Processes in Electrospray Ionization Mass Spectrometry,” *Journal of Mass Spectrometry*, Vol. 35, No. 8, 2000, pp. 939–952.
doi:10.1002/(ISSN)1096-9888
 - [46] Brikner, N., and Lozano, P. C., “The Role of Upstream Distal Electrodes in Mitigating Electrochemical Degradation of Ionic Liquid Ion Sources,” *Applied Physics Letters*, Vol. 101, No. 19, 2012, Paper 193504.
doi:10.1063/1.4766293
 - [47] Enloe, C. L., and Shell, J. R., “Optimizing the Energy Resolution of Planar Retarding Potential Analyzers,” *Review of Scientific Instruments*, Vol. 63, No. 2, 1992, pp. 1788–1791.
doi:10.1063/1.1143339
 - [48] Fedkiw, T. P., “Characterization of an Iodine-Based Ionic Liquid Ion Source and Studies on Ion Fragmentation,” M.S. Thesis, Massachusetts Inst. of Technology, Cambridge, MA, 2010.
 - [49] Prince, B. D., Tirupathi, P., Bemish, R. J., Chiu, Y.-H., and Maginn, E. J., “Molecular Dynamics Simulations of 1-Ethyl-3-Methylimidazolium Bis [(Trifluoromethyl) Sulfonyl] Imide Clusters and Nanodrops,” *Journal of Physical Chemistry, A*, Vol. 119, No. 2, 2015, pp. 352–368.
doi:10.1021/jp507073e
 - [50] Coffman, C., Courtney, D. G., Hicks, F., Jamil, S., Li, H., and Lozano, P., “Progress Toward a Variable Specific Impulse Electrospray Propulsion System,” *47th Joint Propulsion Conference and Exhibit*, AIAA Paper 2011-5591, 2011.

This article has been cited by:

1. Nina Sarah Mühlich, Joachim Gerger, Bernhard Seifert, Friedrich Aumayr. 2022. Simultaneously measured direct and indirect thrust of a FEEP thruster using novel thrust balance and beam diagnostics. *Acta Astronautica* **197**, 107-114. [[Crossref](#)]
2. Xinyu LIU, Hanwen DENG, Yiming SUN, Xiaoming KANG. 2022. Simulation of liquid meniscus formation in the ionic liquid electrospray process. *Plasma Science and Technology* **24**:7, 074008. [[Crossref](#)]
3. Matthew R. Gilpin, Will A. McGehee, N. Ivan Arnold, Michael R. Natisin, Zachary A. Holley. 2022. Dual-axis thrust stand for the direct characterization of electrospray performance. *Review of Scientific Instruments* **93**:6, 065102. [[Crossref](#)]
4. Robert J. Antypas, Kevin D. Sampson, David Torre, Joseph Wang, Large Bradbury-Nielsen Gate Optimized for Electrospray Time of Flight Spectroscopy. *Journal of Propulsion and Power*, ahead of print1-9. [[Abstract](#)] [[Full Text](#)] [[PDF](#)] [[PDF Plus](#)]
5. Yi-Mo Zhang, Zheng-Gang Su, Kang Luo, Hong-Liang Yi. 2022. Transient oscillation response characteristics of an electrohydrodynamic settling drop subjected to a uniform electric field. *Physics of Fluids* **34**:4, 043601. [[Crossref](#)]
6. Chengjin Huang, Jianling Li, Mu Li, Ting Si, Cha Xiong, Wei Fan. 2022. Emission Performance of Ionic Liquid Electrospray Thruster for Micropropulsion. *Journal of Propulsion and Power* **38**:2, 212-220. [[Abstract](#)] [[Full Text](#)] [[PDF](#)] [[PDF Plus](#)]
7. Xinyu LIU, Xiaoming KANG, Hanwen DENG, Yiming SUN. 2021. Energy properties and spatial plume profile of ionic liquid ion sources based on an array of porous metal strips. *Plasma Science and Technology* **23**:12, 125502. [[Crossref](#)]
8. Nakul Nuwal, Victor A. Azevedo, Matthew R. Klosterman, Siddharth Budaraju, Deborah A. Levin, Joshua L. Rovey. 2021. Multiscale modeling of fragmentation in an electrospray plume. *Journal of Applied Physics* **130**:18, 184903. [[Crossref](#)]
9. Daeban Seo, Youngsuk Ryu, Jinnil Choi, Jongkwang Lee. 2021. Design, fabrication, and calibration of a micro-load cell for micro-resistojet development. *Review of Scientific Instruments* **92**:11, 115002. [[Crossref](#)]
10. Chengyu Ma, Thomas Bull, Charles N. Ryan. 2021. Plume Composition Measurements of a High-Emission-Density Electrospray Thruster. *Journal of Propulsion and Power* **37**:6, 816-831. [[Abstract](#)] [[Full Text](#)] [[PDF](#)] [[PDF Plus](#)]
11. Senwen Xue, Li Duan, Qi Kang. 2021. Fabrication of externally wetted emitter for ionic liquid electrospray thruster by low-speed wire cutting combined with electrochemical etching. *AIP Advances* **11**:11, 115023. [[Crossref](#)]
12. Chengjin HUANG, Jianling LI, Mu LI. 2021. Performance measurement and evaluation of an ionic liquid electrospray thruster. *Chinese Journal of Aeronautics* **114**. . [[Crossref](#)]
13. N. M. Uchizono, A. L. Collins, C. Marrese-Reading, S. M. Arestie, J. K. Ziemer, R. E. Wirz. 2021. The role of secondary species emission in vacuum facility effects for electrospray thrusters. *Journal of Applied Physics* **130**:14, 143301. [[Crossref](#)]
14. Hanwu JIA, Maolin CHEN, Xuhui LIU, Chong CHEN, Haohao ZHOU, Hao ZHAO, Zhicong HAN. 2021. Experimental study of a porous electrospray thruster with different number of emitter-strips. *Plasma Science and Technology* **23**:10, 104003. [[Crossref](#)]
15. Yuntian Yang, Dawei Guo, Xiaokang Li, Leimin Deng, Bixuan Che, Mousen Cheng. 2021. Development and Characterization of a Novel Porous-Media Borosilicate Glass Ion Sources for Electrospray Thruster. *Aerospace* **8**:10, 297. [[Crossref](#)]
16. Michael R. Natisin, Henry L. Zamora, Zachary A. Holley, N. Ivan Arnold, Will A. McGehee, Michael R. Holmes, Daniel Eckhardt. 2021. Efficiency Mechanisms in Porous-Media Electrospray Thrusters. *Journal of Propulsion and Power* **37**:5, 650-659. [[Abstract](#)] [[Full Text](#)] [[PDF](#)] [[PDF Plus](#)]
17. Amelia D. Greig, Antonio B. Robali, Catherine M. Carrillo, Alberto Meza. Design and Testing of a CubeSat Rail Integrated Electrospray Thruster . [[Abstract](#)] [[PDF](#)] [[PDF Plus](#)]
18. Peter Wright, Richard E. Wirz. Transient Flow in Porous Electrospray Emitters . [[Abstract](#)] [[PDF](#)] [[PDF Plus](#)]
19. Peter Mallalieu, Manish Jugroot. Investigation of Droplet Mode Electrospray Emitters for use in Multimodal Systems for Spacecraft . [[Abstract](#)] [[PDF](#)] [[PDF Plus](#)]
20. Timothy Fedkiw, Zackary D. Wood, Nathaniel R. Demmons. Improved Computed Tomography Current Mapping of Electrospray Thrusters . [[Abstract](#)] [[PDF](#)] [[PDF Plus](#)]
21. Huiyan Weng, Guobiao Cai, Lihui Liu, Hongru Zheng, Mingxing Zhang, Baiyi Zhang, Bijiao He. 2021. Modifying the theoretical model of the target indirect measurement method for measuring the thrust of electric propulsion. *Measurement Science and Technology* **32**:8, 085301. [[Crossref](#)]

22. Kanta Suzuki, Masayoshi Nagao, Yongxun Liu, Katsuhisa Murakami, Sommawan Khumpuang, Shiro Hara, Yoshinori Takao. 2021. Fabrication of nano-capillary emitter arrays for ionic liquid electrospray thrusters. *Japanese Journal of Applied Physics* **60**:SC, SCCF07. [[Crossref](#)]
23. C. Ma, C. Ryan. 2021. Plume particle energy analysis of an ionic liquid electrospray ion source with high emission density. *Journal of Applied Physics* **129**:8, 083302. [[Crossref](#)]
24. Chong Chen, Maolin Chen, Wei Fan, Haohao Zhou. 2021. Effects of non-uniform operation of emission sites on characteristics of a porous electrospray thruster. *Acta Astronautica* **178**, 192-202. [[Crossref](#)]
25. Peter L. Wright, Richard E. Wirz. 2021. Multiplexed electrospray emission on a porous wedge. *Physics of Fluids* **33**:1, 012003. [[Crossref](#)]
26. Jared M. Magnusson, Adam L. Collins, Richard E. Wirz. 2020. Polyatomic Ion-Induced Electron Emission (IIEE) in Electrospray Thrusters. *Aerospace* **7**:11, 153. [[Crossref](#)]
27. M R Natisin, H L Zamora, W A McGehee, N I Arnold, Z A Holley, M R Holmes, D Eckhardt. 2020. Fabrication and characterization of a fully conventionally machined, high-performance porous-media electrospray thruster. *Journal of Micromechanics and Microengineering* **30**:11, 115021. [[Crossref](#)]
28. Nolan M. Uchizono, Adam L. Collins, Anirudh Thuppul, Peter L. Wright, Daniel Q. Eckhardt, John Ziemer, Richard E. Wirz. 2020. Emission Modes in Electrospray Thrusters Operating with High Conductivity Ionic Liquids. *Aerospace* **7**:10, 141. [[Crossref](#)]
29. Chong CHEN, Maolin CHEN, Haohao ZHOU. 2020. Characterization of an ionic liquid electrospray thruster with a porous ceramic emitter. *Plasma Science and Technology* **22**:9, 094009. [[Crossref](#)]
30. Anirudh Thuppul, Peter L. Wright, Adam L. Collins, John K. Ziemer, Richard E. Wirz. 2020. Lifetime Considerations for Electrospray Thrusters. *Aerospace* **7**:8, 108. [[Crossref](#)]
31. Bryan Little, Manish Jugroot. 2020. Bimodal Propulsion System for Small Spacecraft: Design, Fabrication, and Performance Characterization. *Journal of Spacecraft and Rockets* **57**:4, 707-719. [[Abstract](#)] [[Full Text](#)] [[PDF](#)] [[PDF Plus](#)]
32. Xinyu Liu, Weiguo He, Xiaoming Kang, Mingming Xu. 2019. Fabrication of porous emitters for ionic liquid ion source by wire electrical discharge machining combined with electrochemical etching. *Review of Scientific Instruments* **90**:12, 123304. [[Crossref](#)]
33. Naoki Inoue, Masayoshi Nagao, Katsuhisa Murakami, Sommawan Khumpuang, Shiro Hara, Yoshinori Takao. 2019. Fabrication of a high-density emitter array for electrospray thrusters using field emitter array process. *Japanese Journal of Applied Physics* **58**:SE, SEEG04. [[Crossref](#)]
34. Fiona Leverone, Angelo Cervone, Eberhard Gill. 2019. Cost analysis of solar thermal propulsion systems for microsatellite applications. *Acta Astronautica* **155**, 90-110. [[Crossref](#)]
35. Kui Zeng, Baolin Wu, Yunhai Geng. 2018. Two-phase shaping approach to low-thrust trajectories design between coplanar orbits. *Advances in Space Research* **62**:3, 593-613. [[Crossref](#)]
36. Alexander M. Powaser, Amelia D. Greig. Colloid Thruster to Teach Advanced Electric Propulsion Techniques to Undergraduates . [[Citation](#)] [[PDF](#)] [[PDF Plus](#)]
37. Daniel G. Courtney, Nereo Alvarez, Nathaniel R. Demmons. Electrospray Thrusters for Small Spacecraft Control: Pulsed and Steady State Operation . [[Citation](#)] [[PDF](#)] [[PDF Plus](#)]
38. Igor Levchenko, Kateryna Bazaka, Yongjie Ding, Yevgeny Raitses, Stéphane Mazouffre, Torsten Henning, Peter J. Klar, Shunjiro Shinohara, Jochen Schein, Laurent Garrigues, Minkwan Kim, Dan Lev, Francesco Taccogna, Rod W. Boswell, Christine Charles, Hiroyuki Koizumi, Yan Shen, Carsten Scharlemann, Michael Keidar, Shuyan Xu. 2018. Space micropropulsion systems for Cubesats and small satellites: From proximate targets to furthestmost frontiers. *Applied Physics Reviews* **5**:1, 011104. [[Crossref](#)]
39. Marsil A.C. Silva, Daduí C. Guerrieri, Angelo Cervone, Eberhard Gill. 2018. A review of MEMS micropropulsion technologies for CubeSats and PocketQubes. *Acta Astronautica* **143**, 234-243. [[Crossref](#)]
40. Torsten Henning, Katharina Huhn, Leonard W. Isberner, Peter J. Klar. 2018. Miniaturized Electrospray Thrusters. *IEEE Transactions on Plasma Science* **46**:2, 214-218. [[Crossref](#)]
41. Kazuma EMOTO, Toshiyuki TSUCHIYA, Yoshinori TAKAO. 2018. Numerical Investigation of Steady and Transient Ion Beam Extraction Mechanisms for Electrospray Thrusters. *TRANSACTIONS OF THE JAPAN SOCIETY FOR AERONAUTICAL AND SPACE SCIENCES, AEROSPACE TECHNOLOGY JAPAN* **16**:2, 110-115. [[Crossref](#)]

42. James A. Nabity, John W. Daily. 2018. Effect of Ionic Liquid Composition on Colloid Thruster Emission and Thrust Performance. *Journal of Propulsion and Power* **34**:1, 260-266. [[Abstract](#)] [[Full Text](#)] [[PDF](#)] [[PDF Plus](#)] [[Supplementary Material](#)]
43. Daniel G. Courtney, Herbert Shea, Kathe Dannenmayer, Alexandra Bulit. 2018. Charge Neutralization and Direct Thrust Measurements from Bipolar Pairs of Ionic Electrospray Thrusters. *Journal of Spacecraft and Rockets* **55**:1, 54-65. [[Abstract](#)] [[Full Text](#)] [[PDF](#)] [[PDF Plus](#)]
44. Akshay Reddy Tummala, Atri Dutta. 2017. An Overview of Cube-Satellite Propulsion Technologies and Trends. *Aerospace* **4**:4, 58. [[Crossref](#)]
45. S. W. Miller, B. D. Prince, R. J. Bemish. 2017. Orthogonal time-of-flight mass spectrometry of an ion beam with a broad kinetic energy profile. *Review of Scientific Instruments* **88**:10, 105111. [[Crossref](#)]
46. Bryan Little, Manish Jugroot. Investigation of an Electrospray within a Cold Gas Nozzle for a Dual-Mode Thruster . [[Citation](#)] [[PDF](#)] [[PDF Plus](#)]
47. Enric Grustan-Gutierrez, Manuel Gamero-Castaño. 2017. Microfabricated Electrospray Thruster Array with High Hydraulic Resistance Channels. *Journal of Propulsion and Power* **33**:4, 984-991. [[Abstract](#)] [[Full Text](#)] [[PDF](#)] [[PDF Plus](#)]
48. Kui Zeng, Yunhai Geng, Baolin Wu. 2017. Shape-based analytic safe trajectory design for spacecraft equipped with low-thrust engines. *Aerospace Science and Technology* **62**, 87-97. [[Crossref](#)]
49. Fernando Mier-Hicks, Paulo C. Lozano. 2017. Spacecraft-Charging Characteristics Induced by the Operation of Electrospray Thrusters. *Journal of Propulsion and Power* **33**:2, 456-467. [[Abstract](#)] [[Full Text](#)] [[PDF](#)] [[PDF Plus](#)]
50. David Krejci, Fernando Mier-Hicks, Robert Thomas, Thomas Haag, Paulo Lozano. 2017. Emission Characteristics of Passively Fed Electrospray Microthrusters with Propellant Reservoirs. *Journal of Spacecraft and Rockets* **54**:2, 447-458. [[Abstract](#)] [[Full Text](#)] [[PDF](#)] [[PDF Plus](#)]